JOURNAL OF GEOPHYSICAL RESEARCH, VOL. 115, B06310, doi:10.1029/2009JB006942, 2010

Click Here for Full Article

Geometry and seismic properties of the subducting Cocos plate in central Mexico

Y. Kim,[1] R. W. Clayton,[1] and J. M. Jackson[1]

Received 31 August 2009; revised 22 December 2009; accepted 25 January 2010; published 17 June 2010.

[1] The geometry and properties of the interface of the Cocos plate beneath central Mexico are determined from the receiver functions (RFs) utilizing data from the Meso America Subduction Experiment (MASE). The RF image shows that the subducting oceanic crust is shallowly dipping to the north at 15° for 80 km from Acapulco and then horizontally underplates the continental crust for approximately 200 km to the Trans-Mexican Volcanic Belt (TMVB). The crustal image also shows that there is no continental root associated with the TMVB. The migrated image of the RFs shows that the slab is steeply dipping into the mantle at about 75° beneath the TMVB. Both the continental and oceanic Moho are clearly seen in both images, and modeling of the RF conversion amplitudes and timings of the underplated features reveals a thin low-velocity zone between the plate and the continental crust that appears to absorb nearly all of the strain between the upper plate and the slab. By inverting RF amplitudes of the converted phases and their time separations, we produce detailed maps of the seismic properties of the upper and lower oceanic crust of the subducting Cocos plate and its thickness. High Poisson's and Vp/Vs ratios due to anomalously low S wave velocity at the upper oceanic crust in the flat slab region may indicate the presence of water and hydrous minerals or high pore pressure. The evidence of high water content within the oceanic crust explains the flat subduction geometry without strong coupling of two plates. This may also explain the nonvolcanic tremor activity and slow slip events occurring in the subducting plate and the overlying crust.

Citation: Kim, Y., R. W. Clayton, and J. M. Jackson (2010), Geometry and seismic properties of the subducting Cocos plate in central Mexico, *J. Geophys. Res.*, *115*, B06310, doi:10.1029/2009JB006942.

1. Introduction

[2] The Cocos plate has been subducting underneath the North American plate in this present geometry at a rate of about 12 cm/yr from 20 Ma to 11 Ma and 6 cm/yr from 11 Ma to present (from EarthByte poles [*Müller et al.*, 2008]). The subduction interface has a strong variation in along-strike dip angles along the central part of Middle American Trench (MAT). To the northwest near the Rivera Plate junction, the dip is 50°, while to the southeast near the Tehuantepec Ridge it is 30° [*Pardo and Suárez*, 1995]. As shown by *Pérez-Campos et al.* [2008], the slab at the central part near Acapulco is horizontal. The along-strike change in dip is evident in the trace/strike of the Neogene volcanic arc (TMVB) which trends at a 17 degree angle to the trace/strike of the trench. At 30 Ma, the volcanism ceased in Miocene arc along the coast, and after 10 Ma hiatus, reappeared just south of Mexico City and proceeded to migrate to the northern end of the TMVB [*Ferrari*, 2004]. Since that time, the slab in central Mexico has been rolling back, as evidenced by the southward migration of TMVB volcanism, to its current location at the south edge of the TMVB.

[3] There have been a number of studies of the Cocos plate subduction especially regarding the slab geometry in central Mexico. *Couch and Woodcock* [1981] described offshore seismic, gravity, and magnetic measurements near Acapulco and suggested a 9 km thick oceanic crust dipping 2° under the continental margin. *Valdes-Gonzalez and Meyer* [1996] provided a model which includes the continental Moho of 45 km and 10° dipping slab with 8 km thickness between the Pacific coast and Mexico City using the Petatlán earthquake aftershocks. *Pardo and Suárez* [1995] described the shallow slab subduction at distances of between 110 km to 275 km from the MAT based on relocated hypocenters of local earthquakes. The work by *Kostoglodov et al.* [2003] further supported the shallow slab subduction by providing a more precise geometry of subducting Cocos plate up to 200 km from the MAT constrained by the seismicity and gravity data. None of the studies resolved the slab geometry underneath the TMVB because there is very little seismicity away from the seismogenic zone adjacent to the trench.

[4] There are several geochemical studies that infer the fate of the descending slab underneath the TMVB (after 250 km

[1]Seismological Laboratory, California Institute of Technology, Pasadena, California, USA.

Copyright 2010 by the American Geophysical Union.
0148-0227/10/2009JB006942

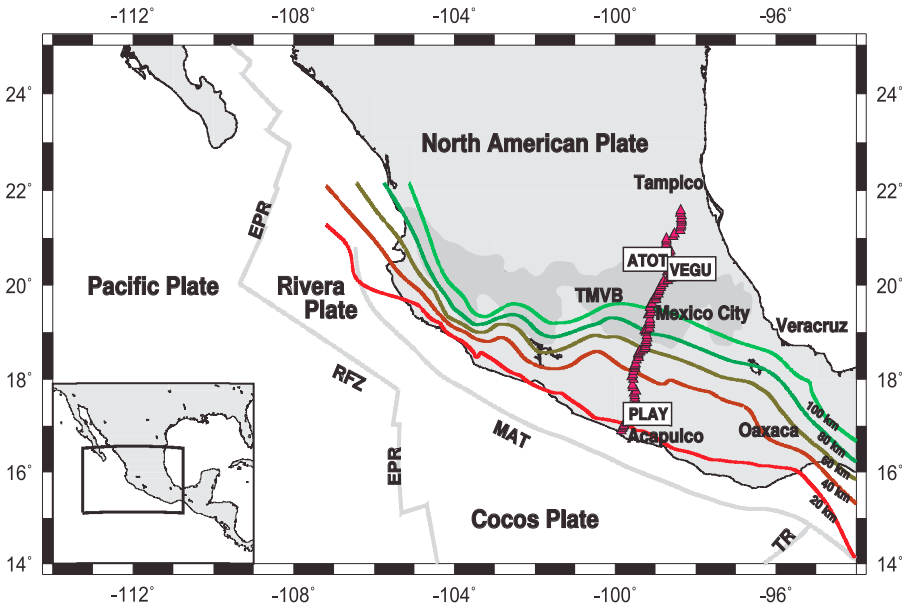

Figure 1. Map showing the region of the study and stations in the MASE array indicated as red triangles. The map includes four lithospheric plates: Pacific, Rivera, Cocos, and North American plates. The abbreviations shown in the map are EPR, East Pacific Rise; MAT, Middle American Trench; RFZ, Rivera Fracture Zone; TR, Tehuantepec Ridge. Dark gray region in the middle of the North American plate is Quaternary volcanic area known as Trans Mexican Volcanic Belt (TMVB). Isodepth contours of the subducted Cocos plate beneath the North American plate [*Pardo and Suárez*, 1995] are shown in the map. Note that the first station of the MASE array is located at Acapulco (~75 km from the MAT) and the horizontal axis of the RF images are all plotted in reference to that station.

from the MAT) after the shallow subduction near the coast. *Ferrari* [2004] proposed a slab detachment model beneath the TMVB to explain a short (2–3 Myr) eastward migrating mafic pulse in the late Miocene based on several volcanic and geochemical features of central Mexico. The tear in the slab due to the strong coupling between the Magdalena microplate and the overriding North American plate propagated eastward [*Ferrari*, 2004]. Lateral propagation of such a slab detachment episode induced hot subslab material to flow into the slab window causing the volcanism with unusual geochemical features for a subduction setting [*Ferrari*, 2004]. Reported adakite observation in the TMVB also supports this. Some adakitic observations are for early Miocene TMVB volcanism [*Gómez-Tuena et al.*, 2008]. *Kay* [1978] first attributed adakites to the interaction of a large ion lithophile element-rich hydrous melt from the subducted oceanic crust with overlying mantle, and then eruption without interaction with the island arc crust. According to *Ferrari et al.* [2001], the lavas with such compositions may have been produced by small amounts of melting of a heterogeneous mantle fluxed by fluids released by the subducting slab.

[5] In 2005, the Meso American Subduction Experiment (MASE) was deployed to image the structure of the system and to provide the parameters for a geodynamical model of the subduction process. Approximately 2 years of broadband seismic data were collected at 100 stations along a 550 km transect through Mexico City from Acapulco on the Pacific side to a point 100 km from the Gulf of Mexico, near Tampico. The north trending transect is oriented nearly perpendicular to the MAT. The geometry of the experiment is shown in Figure 1.

[6] The density of the MASE survey (~6 km station spacing) enables the use of teleseismic converted waves to accurately image the slab and (oceanic and continental) Moho. The receiver functions (RFs) are well suited to constrain the depths of major boundaries such as the top of the subducting slab, the oceanic crust-mantle interface of the slab, and the base of continental crust in the overlying plate. *Pérez-Campos et al.* [2008] provided a back-projected RF image of the slab and crustal structure to a depth of 100 km. In this study, we will show stacked RF images obtained for different back-azimuth event groups. We expand our work on RFs to do a Kirchoff-like migration/inversion using teleseismic earthquakes to image the structures underneath the TMVB to a depth of 250 km. The technique is similar to that used by *Bostock et al.* [2002] for the Cascadia subduction zone. In addition, we provide a seismic velocity model from the finite difference (FD) modeling on the horizontal interface between the lower continental crust and the top of the subducting Cocos plate suggested by *Pérez-Campos et al.* [2008]. Last, we will describe a technique to determine and map seismic properties and thickness of the top interface of the Cocos plate using the P-to-S converted phases.

2. Data Analysis

2.1. Teleseismic Data

[7] The location of the stations in the MASE array is shown in Figure 1. For the RF analysis, the data includes

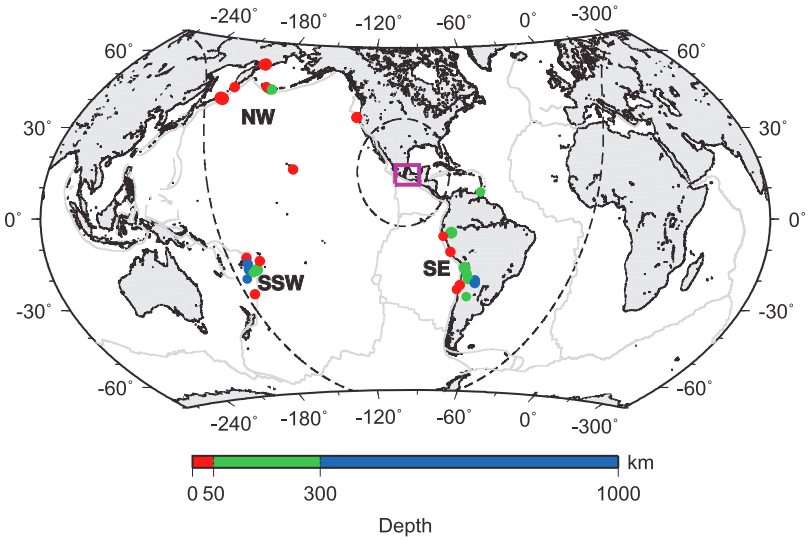

Figure 2. Distribution of teleseismic events used in the study, which includes 12 events in a southeast (SE) back-azimuth band from 139° to 145°, 9 events in a south-southwest (SSW) band from 238° to 250°, and 13 events in a northwest (NW) band from 317° to 330° from the station array enclosed in the purple box. Dashed lines are a distance of 30° and 90° away from Mexico City, the central point of the station array. The events are colored according to depths.

34 earthquakes of magnitude greater than 6.1 that generally occur in three different back-azimuth groups from the MASE array (Figure 2). After a careful selection based on the signal-to-noise ratio, individual waveform data are time windowed to 90 s, band-pass filtered from 0.01 to 1 Hz, and rotated to radial and tangential coordinates. The data recorded over the TMVB, which laterally spans from 240 to 410 km from the Acapulco station, tends to be noisier than the other sites because of the cultural noise (six of the stations are in urban Mexico City), and scattering by the volcanic rocks.

[8] The RFs from each back azimuth are separately stacked to give a better estimate of the averaged Moho depth beneath a station and show the azimuthal variations [*Yan and Clayton*, 2007]. A total of 34 events span epicentral distances from 30° to 90°, which corresponds to ray parameters from 0.04 to 0.08 s/km. The data are selected if the signal-to-noise ratio is greater than a factor of 3 on the vertical component. Of the total 34 events, 12 events are selected within a SE back-azimuth band from 139° to 145° from the MASE array; 9 events within a SSW band from 238° to 250°; and 13 events within a NW band from 317° to 330°.

2.2. Receiver Function Analysis

[9] Standard RF processing enhances P-to-S converted phases by removing source complexities through the deconvolution of radial component seismograms by corresponding vertical components. Two types of deconvolution techniques are used in the analysis: (1) the frequency domain deconvolution [*Langston*, 1979; *Ammon et al.*, 1990] and (2) the iterative time domain deconvolution technique [*Kikuchi and Kanamori*, 1982; *Ligorria and Ammon*, 1999]. The major converted phases in the RFs are observed with both methods for data with high signal-to-noise ratio, but we find that the time domain deconvolution provides the highest resolution for sharply constraining the geometry of the slab and Moho above 100 km depth. The frequency domain deconvolution works better with low-frequency components, but it enhances the strength of the multiples. As an example, Figure 3 shows the vertical component seismograms along with the RFs using the time domain deconvolution. Figure 4 shows radial and tangential RFs for stations ATOT and VEGU (located in Figure 1), plotted according to the back azimuth. Note that the amplitude of tangential RFs is smaller by a factor of 2 compared to that of radial RFs. A detailed analysis of the tangential component is given by *Greene* [2009].

[10] All the reflected/converted modes exhibit a distinct moveout as a function of source-receiver offset. By measuring these moveouts (assuming a locally flat layered structure), it is possible to estimate local depth and average Vp/Vs ratio between the surface and the discontinuity associated with each mode [*Zhu and Kanamori*, 2000]. In practice, individual modes can be difficult to observe and identify on individual traces, so stacking many events at similar distances and back azimuths is employed, and a search is performed over a range of depths to the discontinuity and Vp/Vs ratios. Uncertainty estimates on the crustal thickness and the Vp/Vs ratio for the grid search algorithm are estimated from by the 95% confidence interval. As an example of this stacking method, Figure 5 shows RF seismograms and the resulting stack, and the contour map of depth and Vp/Vs ratio for stations ATOT and PLAY (located in Figure 1).

[11] RFs calculated at individual stations can be used to map out features such as Moho topography and slab structure across an array. Figure 6 shows the RF cross section

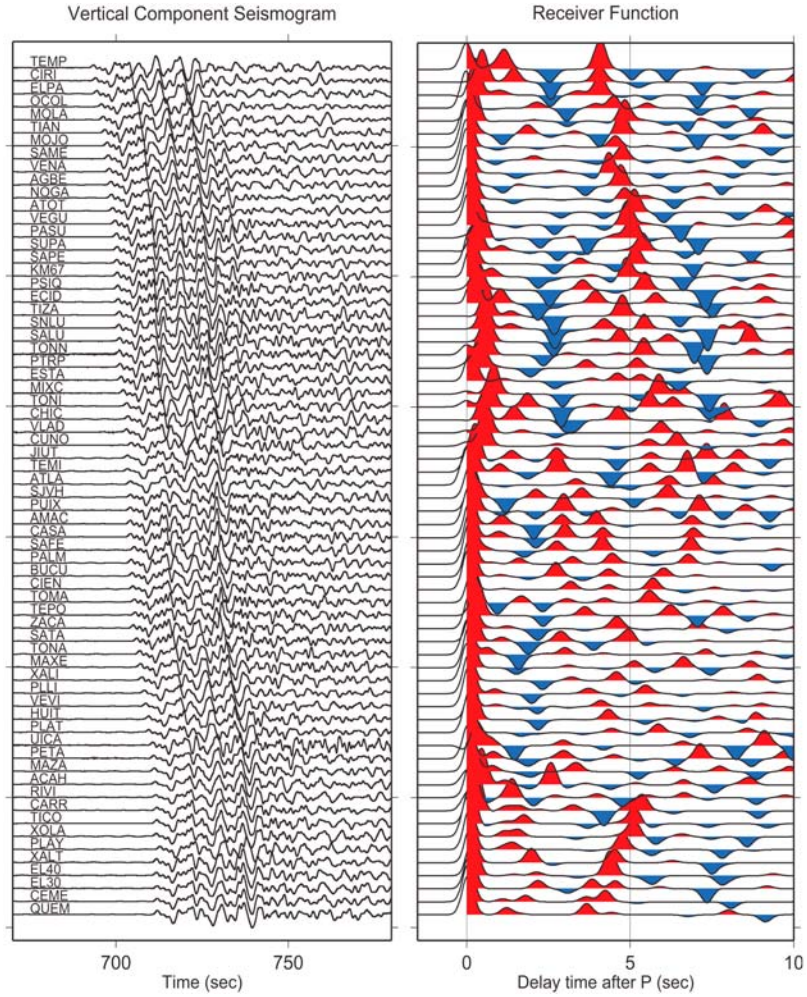

Figure 3. A record section of (left) the vertical component seismograms and (right) the corresponding RFs, obtained by processing the event on 20 April 2006 recorded from the MASE array. The seismograms and RFs are aligned in the order of increasing station latitude from bottom to top.

obtained by evaluating the 21 March 2005 event recorded at stations from the Acapulco station (~75 km from the trench) to inland before the TMVB. The image shows the slab interface with a distinct negative pulse (blue) over a positive (red) pulse starting at 15 km depth at the Acapulco station. It dips down 15° to a point 80 km from the Acapulco station and then runs horizontally for 120 km. This horizontal section of the slab underplates the continental crust and ends just before the TMVB. The negative RF pulse indicates an existence of the low-velocity layer at the top part of the subducting oceanic crust. Details on this low-velocity layer are discussed in sections 2.4 and 2.5.

[12] Figure 7 shows a stacked RF cross section from each back-azimuth event group (SE, NW, and SSW) recorded at all the stations. The stacked RF from each direction enhances different part of the slab and Moho due to 3-D heterogeneities in the crust. For all three images in Figure 7, we observe the horizontal interface of the subducting Cocos plate indicated by the negative (blue) pulse followed by the oceanic Moho by the positive (red) pulse after an initial dip of 15° at 5 to 6 s (~40 to 50 km in depth) and a lateral distance of 80 to 225 km from the Acapulco station. Furthermore, the RFs, especially from Acapulco to a point 100 km to the north in the continental crust, show horizontal layers of the negative and positive RF pulses (Figure 8). We determine the mechanism for the crust attenuation at the trench end of the slab to be undersided erosion by the slab and not uplift by the slab followed by surface erosion. The crustal thickness before the TMVB is 45 km on average, agreeing with the seismic refraction data and gravimetric studies [*Jording et al.*, 2000; *Valdes-Gonzalez and Meyer*, 1996].

[13] For all the back-azimuth groups, the midsection beneath the TMVB exhibits a relatively flat and strong Moho varying slowly in depth between 38 and 43 km (Figure 7). There is no apparent thickening of the crust under the TMVB. If the topography of the TMVB (2.2 km) were compensated by an Airy mechanism, one would expect a root of approximately 13 km beneath it. Underneath the TMVB, a strong low-velocity zone is present at 3 s (~25 km in depth) indicating partial melting features (Figure 7). This is in agreement with the shear wave velocity results pre-

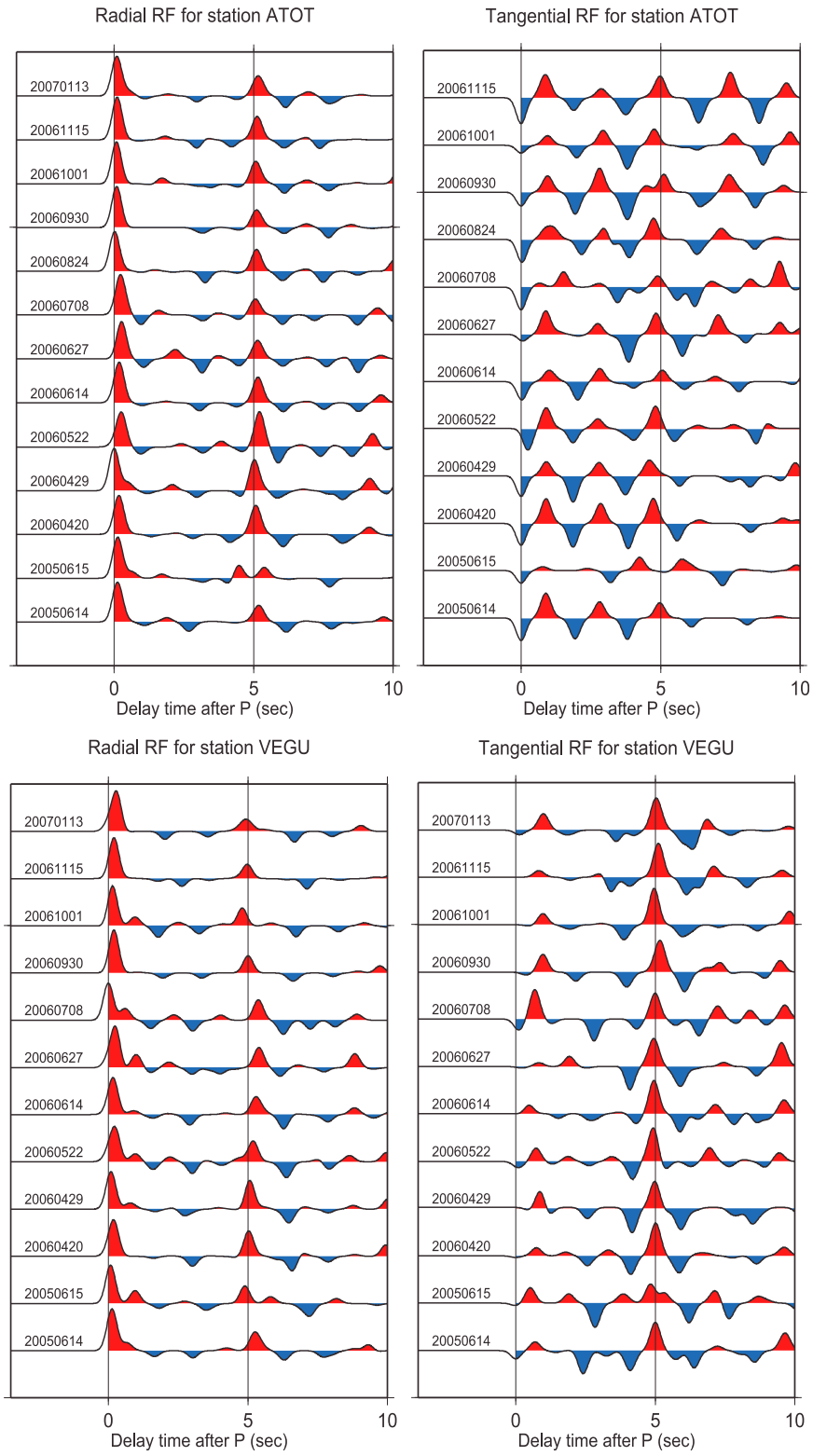

Figure 4. Radial and tangential RFs for station ATOT and VEGU. Each event date is indicated at the left of each trace. Ps conversion from Moho (the second largest peaks in radial RFs) arrives at 5 s for both stations. For comparison purposes, we boost amplitudes of the tangential RFs by a factor of 2.

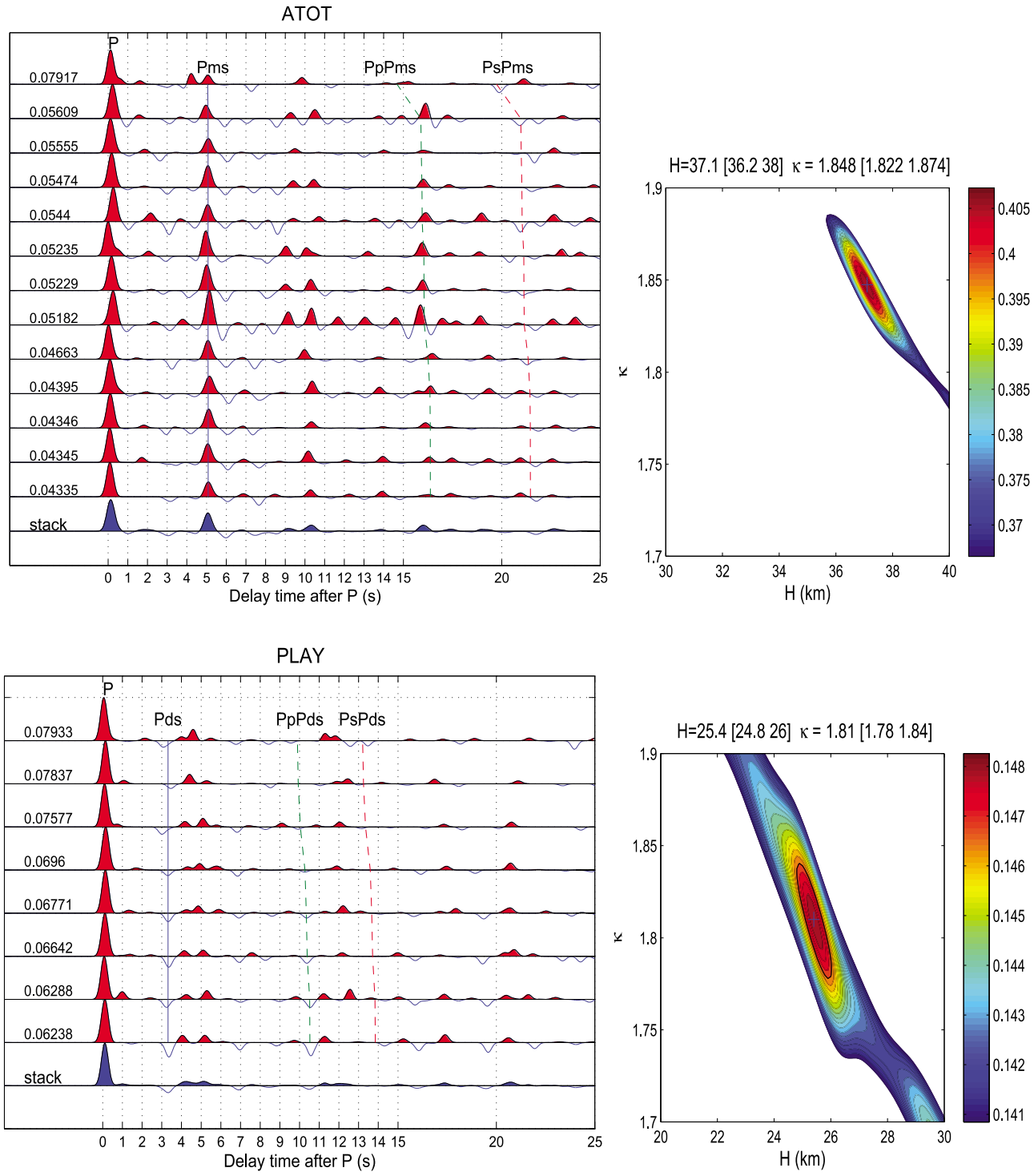

Figure 5. Crustal thickness (Moho, discontinuity depth H) and Vp/Vs ratio (κ) for stations (top) ATOT and (bottom) PLAY. (left) RF traces sorted according to the ray parameter indicated at the left of each RF trace. The predicted arrival times of the primary phase ((top) Pms and (bottom) Pds) and two multiples ((top) PpPms and PsPms and (bottom) PpPds and PsPds) are marked by the solid and dashed lines. (right) Contour map of the weighted summation function [*Zhu and Kanamori*, 2000] for the discontinuity depth (H) and Vp/Vs ratio (κ). The black cross is the picked H and κ, which maximize the summation function, and the black line is the 95% confidence bound, which represents their uncertainty estimate.

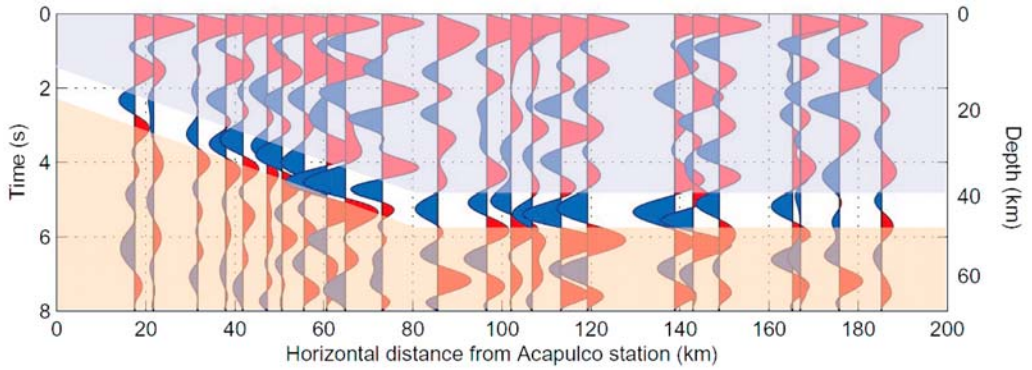

Figure 6. RF cross section showing the subducting Cocos plate using stations from Acapulco (~75 km from the trench) to the start of the TMVB. The single event that occurred on 21 March 2005 is processed by the frequency domain deconvolution. The blue, white, and orange overlays denote the continental crust, oceanic crust, and oceanic lithosphere, respectively.

sented by *Iglesias et al.* [2010] from surface wave studies. They propose that reduced velocities may correspond to reduced densities and hence provide a Prett type compensation method for the TMVB. High Vp/Vs ratio of 1.806 (Poisson's ratio of 0.279) is estimated for the TMVB, which may indicate an overall more mafic crustal composition [*Zandt and Ammon*, 1995]. In addition, the crustal Vp/Vs ratios for the whole profile range from 1.65 to 1.898 with an overall average crustal Vp/Vs ratio of 1.79 (Poisson's ratio of 0.273). North of the TMVB, the crust thins from 35 to 25 km toward the end of the MASE array.

[14] For all the back-azimuth groups, the geometry of the slab plunging into the mantle underneath the TMVB is less well determined. The thick red P pulses in the TMVB are likely caused by resonances in basins such as the Valle of Mexico. Strong lateral velocity contrasts at the vicinity of the mantle wedge, including the oceanic plate projecting into the mantle, would further complicate the waveforms.

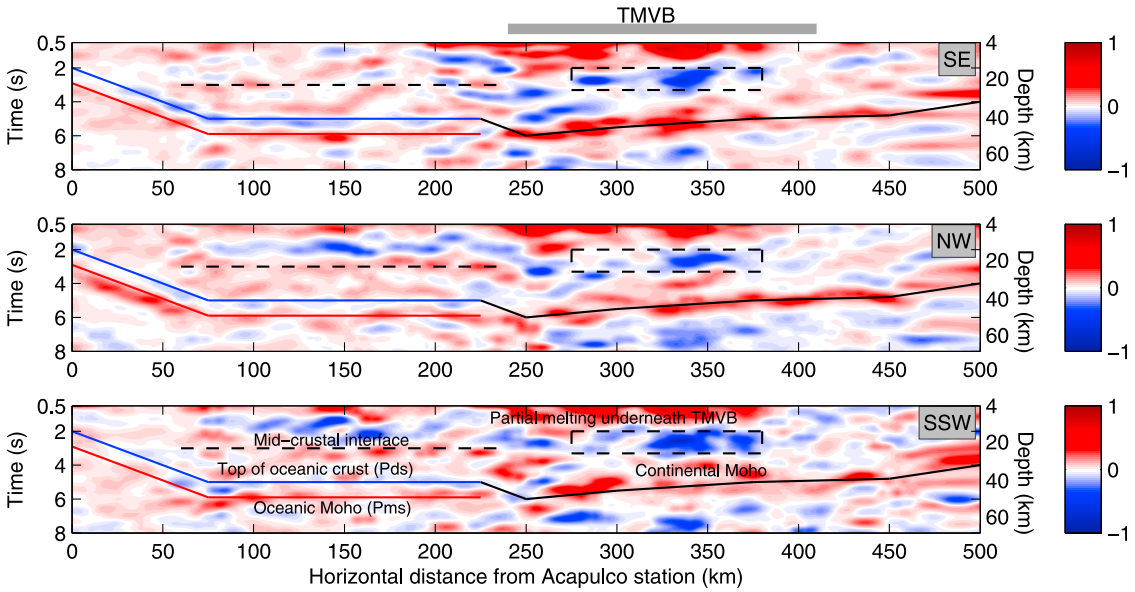

Figure 7. Stacked RF images for (top) SE, (middle) NW, and (bottom) SSW back azimuths. The RFs are computed by the iterative time domain deconvolution [*Kikuchi and Kanamori*, 1982; *Ligorria and Ammon*, 1999]. Each image is created by assigning RF amplitudes into a separate output grid and filling the missing data by the linear interpolation. Note that the image is not sharply constrained from 450 km to the end of the array (~533 km) in the horizontal axis because the data sparsely are spaced at the northern section. The RFs in the SSW group are relatively noisier possibly because of the complications in the earthquake source and travel paths of seismic waves. Note that the P phase at zero second (the largest peak at the RF) is removed in the image to enhance the smaller signals after P. The color bar denotes the normalized RF amplitude. An uninterpreted display is given in Figure A1.

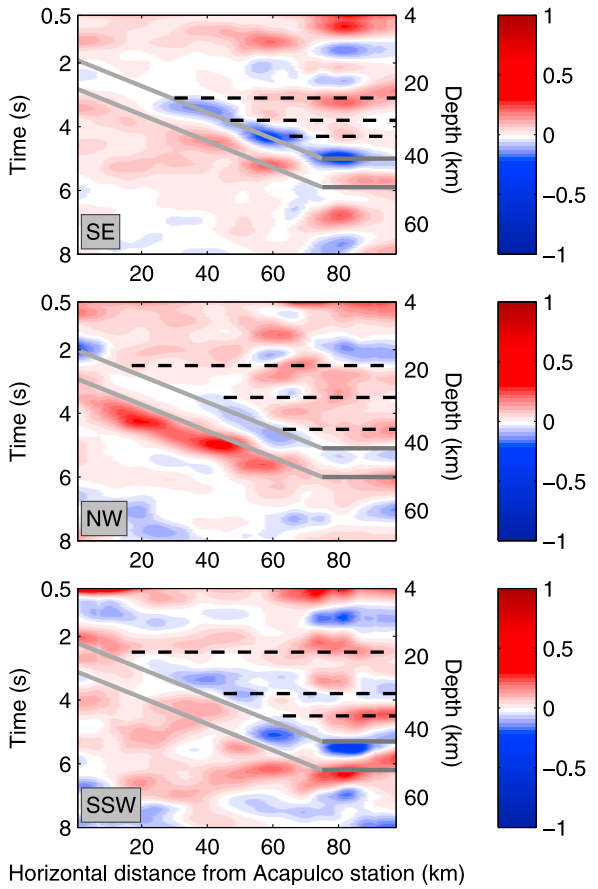

Figure 8. RF images for (top) SE, (middle) NW, and (bottom) SSW back azimuths for 0.5–8 s and 0–95 km from the Acapulco station. Positive and negative RF amplitudes (indicated as dashed lines) above the subhorizontal oceanic crust are roughly parallel to its horizontal interface indicated as dark gray lines and not the shallow dipping oceanic crust indicated as light gray lines. The mechanism for such crust attenuation near the coast is thus determined to be undersided erosion by the oceanic crust and not uplift by the slab followed by the surface erosion. The color bar denotes the normalized RF amplitude. An uninterpreted display is given in Figure A2.

P wave tomographic images provided by *Gorbatov and Fukao* [2005] and *Husker and Davis* [2009] showed that the slab is dipping in 90° and 75°, respectively. The RF method is not capable of detecting such near-vertical structures (see section 2.4 for details).

2.3. Receiver Function Imaging

[15] The dense station spacing (6 km on average) is well suited for applying more accurate seismic migration techniques to teleseismic RF imaging. The method behind the inversion of the teleseismic waves and detailed discussion are given by *Bostock et al.* [2001]. Here, we migrate the P-to-S converted phases (Pds, conversion from the top of the oceanic crust to the base of the continental crust, and Pms, conversion from the mantle to the bottom of the oceanic crust) using a Kirchhoff-style migration, which characterizes the output model as a grid of point scatterers. We assume that teleseismic P waves are arriving sufficiently far away that they can be approximated by plane waves. Traveltimes for the P-to-S converted waves are calculated by assuming that the incident plane P wave converts to S wave energy at every possible scattering point (see Figure 9, top). Figure 9 (bottom) shows the traveltime curves for the converted phase at one scattering point for varying incident angles of the plane wave. After determining the traveltimes of the converted wavefields at the scattering point, corresponding amplitudes are stacked to form an image. A similar procedure can be used for the multiples as was done by *Bostock et al.* [2002], but in our case the multiples are very weak, and do not contribute significantly to the image.

[16] Figure 10 shows a migrated image from the direct P-to-S converted phases of all 34 teleseismic events. We use a simple layer velocity model to compute traveltimes

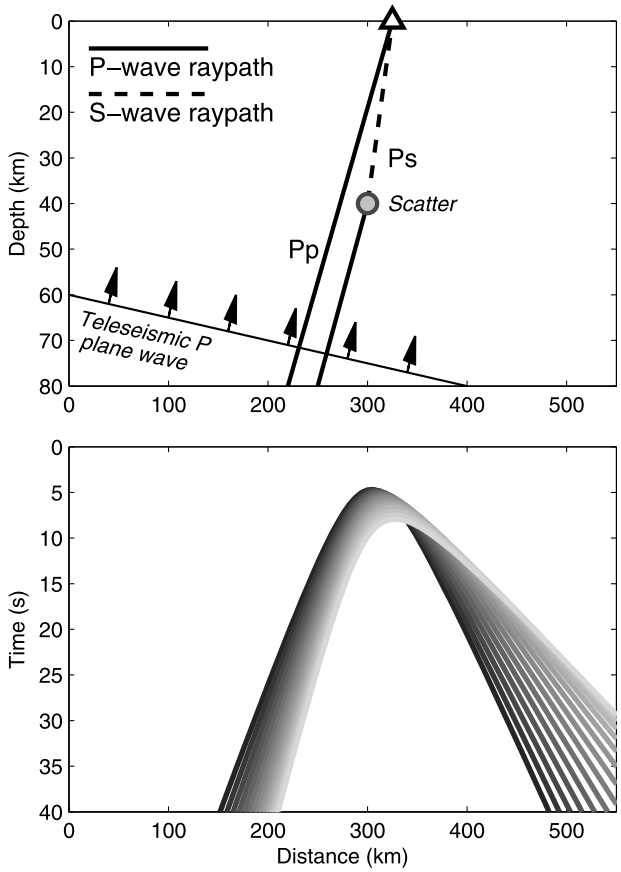

Figure 9. Schematic view of showing (top) a plane wave that travels from below and converts into converted phases such as Pms and Pds at the scattering point and (bottom) the traveltime curve for Ps wave by varying the incidence angle of the plane wave and fixing the scattering point. For the traveltime calculation, the scattering point is fixed at (300 km, 40 km), and the P and S wave velocities are 6.3 and 3.6 km/s, respectively. The incident angle is varied from 10° to 80° in every 5°. Each line is shaded according to the incident angle, and its lighter color corresponds to larger incident angle.

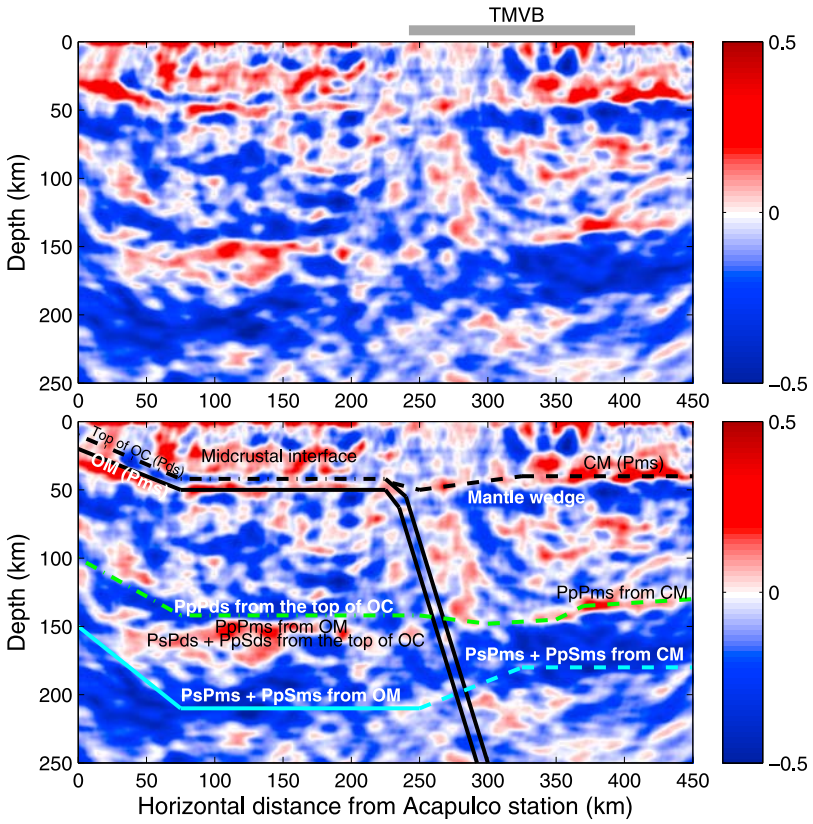

Figure 10. Migrated image of (top) uninterpreted display and (bottom) interpreted display using Pms and Pds phases, showing the steeply dipping oceanic crust at about 75° underneath the TMVB. The dash-dotted lines indicate the top of the subducting oceanic crust characterized by the very low velocity. The dashed line indicates the continental Moho, which extends from TMVB to the coast near Gulf of Mexico. Seismic multiples from oceanic Moho (OM) and continental Moho (CM) as well as the subhorizontal oceanic crust are shown clearly in the image. Note that the green (dash-dotted and dashed) lines are the multiples from the crustal interface (Pds and Pms), and the cyan (solid and dashed) lines are the multiples from the oceanic and continental Moho. Subducting Cocos plate is located by changes in the depth of the seismic multiple changes. Note that the image does not include the section from 450 km to the end of the array (~533 km) in the horizontal axis because the data are sparsely spaced at the northern section. The color bar denotes the normalized RF amplitude.

for the converted wave according to the raypath geometries specified in Figure 9. Several velocity sensitivity tests were performed to find that the energy is sharply focused when the average crustal P wave velocity is 6.3 km/s and S wave velocity is 3.6 km/s. The dip and depth of the subducting oceanic crust and the oceanic Moho before the TMVB as determined from the imaging are in good agreement with the RF images shown in Figure 7. The crustal interfaces at depths of 25 km and 30 km above the horizontal oceanic crust are observed. The continental Moho is clearly shown from the beginning of the TMVB to 450 km in lateral distance. The migration enhances the strength of the seismic multiples (PpP(d,m)s, PsP(d,m)s, and PpS(d,m)s).

[17] The image beneath the TMVB shows that the slab plunges steeply (~75°) in the mantle at 250 km from the Acapulco station, which agrees well with the tomography result provided by *Husker and Davis* [2009]. The location of the steeply dipping slab can also be easily traced from the place where the depths of the seismic multiples abruptly change at 250 to 300 km in lateral distance (Figure 10). The positions of the multiples (PpPms, PsPms, and PpSms) are elevated when transitioning from the oceanic Moho to the continental Moho (Figure 10). The dip of the slab is more apparent in the migrated image despite the noisy RFs obtained from the stations in the TMVB.

2.4. Receiver Function Finite Difference Modeling

[18] To further investigate the images, we produce synthetic RFs with a 2-D finite difference wave propagation program for particular velocity and slab geometry models and compare these to the data. The laterally complicated structure (continental crust, oceanic crust, and mantle before the TMVB and continental crust, mantle wedge, oceanic crust, and mantle underneath and after the TMVB), leads to very complicated images containing Pds and Pms phases, and their seismic multiples. The FD modeling helps verify several seismic phases due to the complicated structure present underneath the MASE array. In this section, we

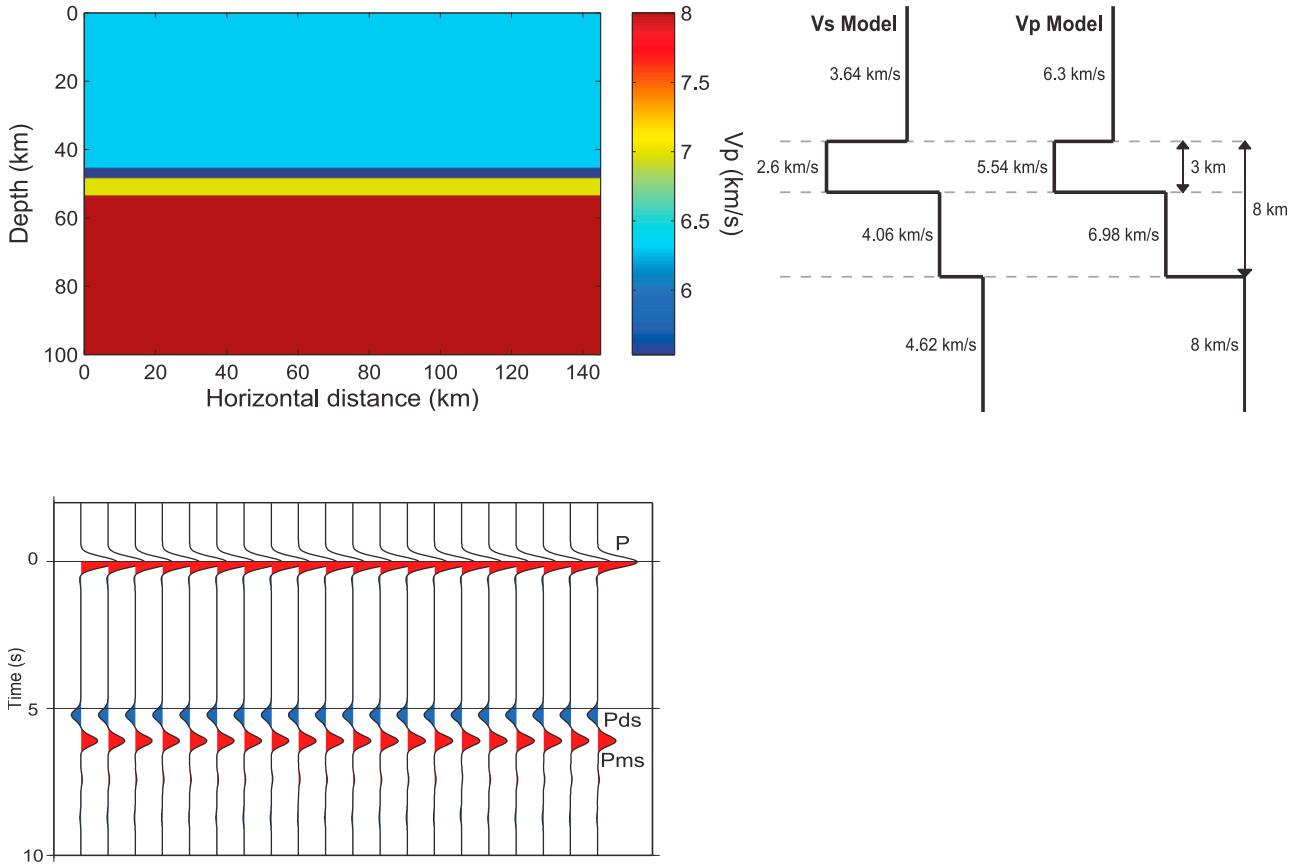

Figure 11. (top left) P wave velocity model, (top right) P and S wave velocity models, and (bottom) corresponding synthetic RFs for the subhorizontal part of the Cocos plate subduction south of the TMVB.

show one velocity model to represent our horizontal oceanic crust before the TMVB.

[19] On the basis of our observations in sections 2.2 and 2.3, the model consists of an average crust of 45 km, an oceanic crust, which runs horizontally for 145 km, and a mantle zone prior to the oceanic crust diving into the mantle (see the P wave model in Figure 11). Delays between the direct and converted wave are proportional to the depth of the interface and depend on the transmission velocities along their paths, while the amplitude of the converted arrival depends on the magnitude and sign of the velocity contrast. Thus, the thickness and the RF amplitude peak-to-peak height of the oceanic crust are used as additional constraints to construct the model. To match the negative (blue) and positive (red) RF pulses at 5 and 6 s, respectively, from Figure 6, the oceanic crust should be characterized as a low-velocity layer above the mantle. However, a single layer cannot reproduce the amplitudes of the positive and negative pulses, so it is further divided into two low-velocity layers to achieve a comparable (but opposite in polarity) velocity contrast that we see from the 1 s RF data (Figure 6). The additional low-velocity zone (denoted hereafter as upper oceanic crust) includes velocities much lower that normal oceanic crustal velocities (of the lower oceanic crust). *Song et al.* [2009] also inserted the ultraslow velocity layer (S wave velocity of 2.0 to 2.7 km/s) over the low-velocity layer in their model to reproduce the converted SP arrivals and teleseismic underside reflections from the top of the subducting plate. In the P and S wave velocity model (Figure 11), the upper oceanic crust has the thickness of 3 km, the P wave velocity of 5.54 km/s, and S wave velocity of 2.6 km/s; the lower oceanic crust the thickness of 5 km, the P wave velocity of 6.98 km/s, and S wave velocity of 4.06 km/s. Plane waves with variable incident angles in the range of 0.04 to 0.08 are then entered as boundary conditions on left bottom corner of our constructed model. Iterative time domain deconvolution [*Kikuchi and Kanamori*, 1982; *Ligorria and Ammon*, 1999] is used to convert the synthetic seismograms to the radial RFs (Figure 11).

[20] Figure 12 shows result of a dip sensitivity test. We vary the dip from shallow to steep angles (10°, 25°, 50°, and 75°), using the same velocity model specified in Figure 11, and observe how the RF image reproduces the dipping slab. When the dip angle exceeds 50°, the polarity of the synthetic RFs changes the sign, in agreement with the change in sign of the transmission coefficient. This explains why we do not see a clear image of the slab descending into the mantle in 75° from Figure 7. The effect of the sign change is not included in the migrated image (Figure 10).

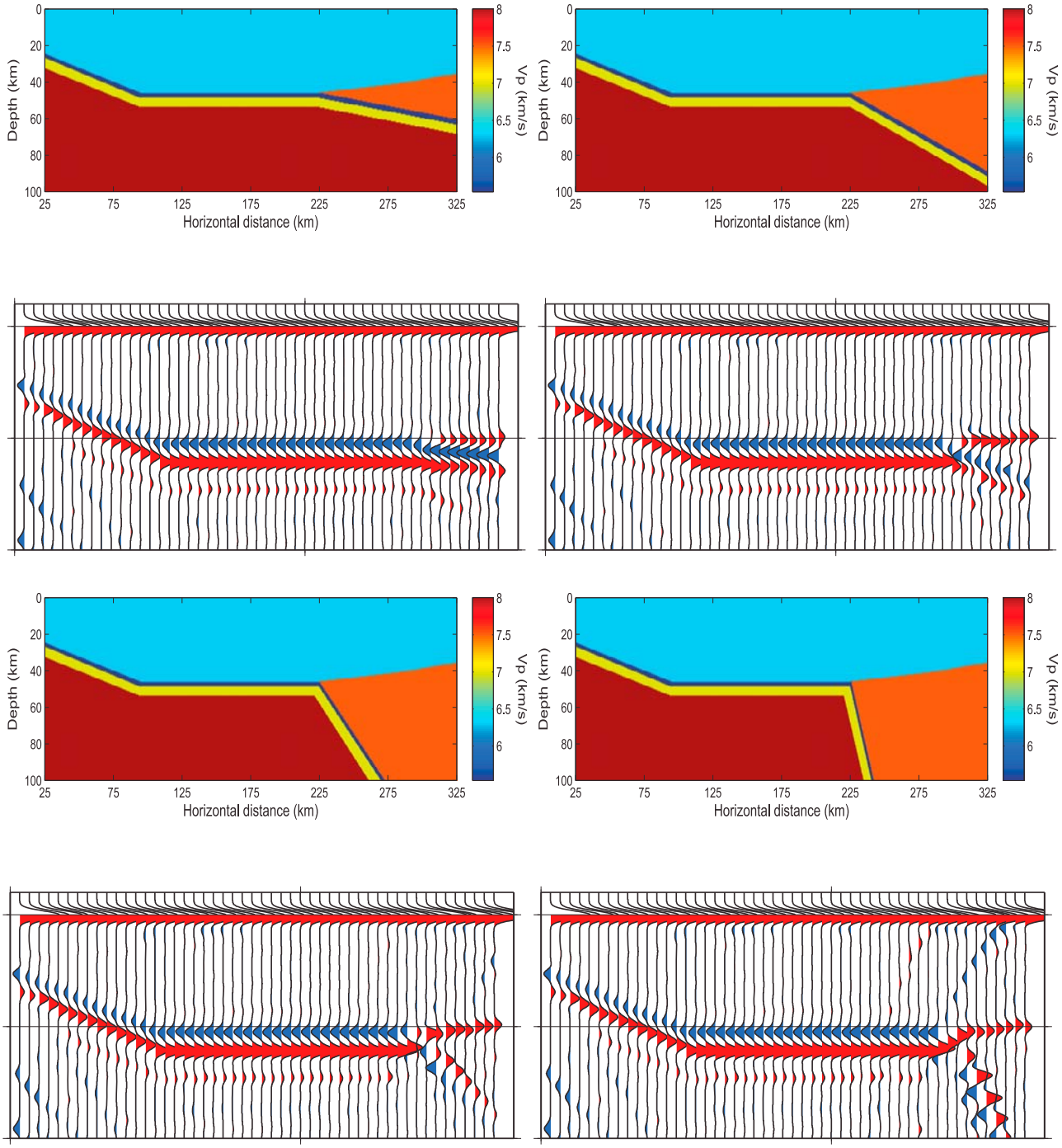

Figure 12. Dip sensitivity test results using 2-D finite difference modeling to demonstrate that RFs at steeper angles do not work. The dip angles vary from 10°, 25°, 50°, to 75°. Note that the polarity of the synthetic RFs changes the sign when the dip angle exceeds 50°. Also, the diffraction artifact from a sharp corner appears to be strong in the overlying crust.

2.5. Inversion of Receiver Function Amplitudes

[21] The FD modeling result in section 2.4 reveals that low P and S wave velocity layer is necessary to reproduce a strong negative impedance contrast seen at the top of the subducting oceanic crust in our 1 s RF data set. To further investigate the nature of our upper and lower oceanic crust, we develop a technique based on plane wave conversion to invert the seismic parameters such as impedance (a product of S wave velocity and density). The method utilizes the RF amplitude information of the P-to-S converted phases (Pds and Pms) in the four-layer model (crust, upper and lower

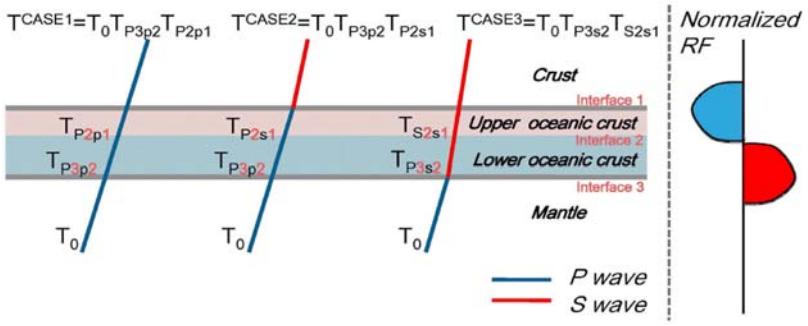

Figure 13. Schematic showing transmitted responses at top and bottom interfaces of the oceanic crust. The RF responses responses are normalized by the P arrival. The peak of the negative RF pulse is obtained at the interface 1 between the crust and the upper oceanic crust; the peak of the positive RF pulse at the interface 3 between the lower oceanic crust and the mantle.

oceanic crust, and mantle) and leads to an estimation of the seismic properties of the upper and lower oceanic crust.

[22] We obtain three different cases when the P wave is transmitted as a P or S wave at the top and bottom of the oceanic crust as shown in Figure 13. The case 1 is when there is no conversion; the case 2 when the P wave is converted into S wave at the top of the (upper) oceanic crust; and the case 3 when the P wave is converted into S wave at the bottom of the (lower) oceanic crust. By denoting the transmission coefficient at the interface as T for simplicity, we can express the transmission coefficient for each case as

$$T^{\mathrm{CASE1}} = T_0 T_{P3p2} T_{P2p1}, \tag{1}$$

$$T^{\mathrm{CASE2}} = T_0 T_{P3p2} T_{P2s1}, \tag{2}$$

$$T^{\mathrm{CASE3}} = T_0 T_{P3s2} T_{S2s1}, \tag{3}$$

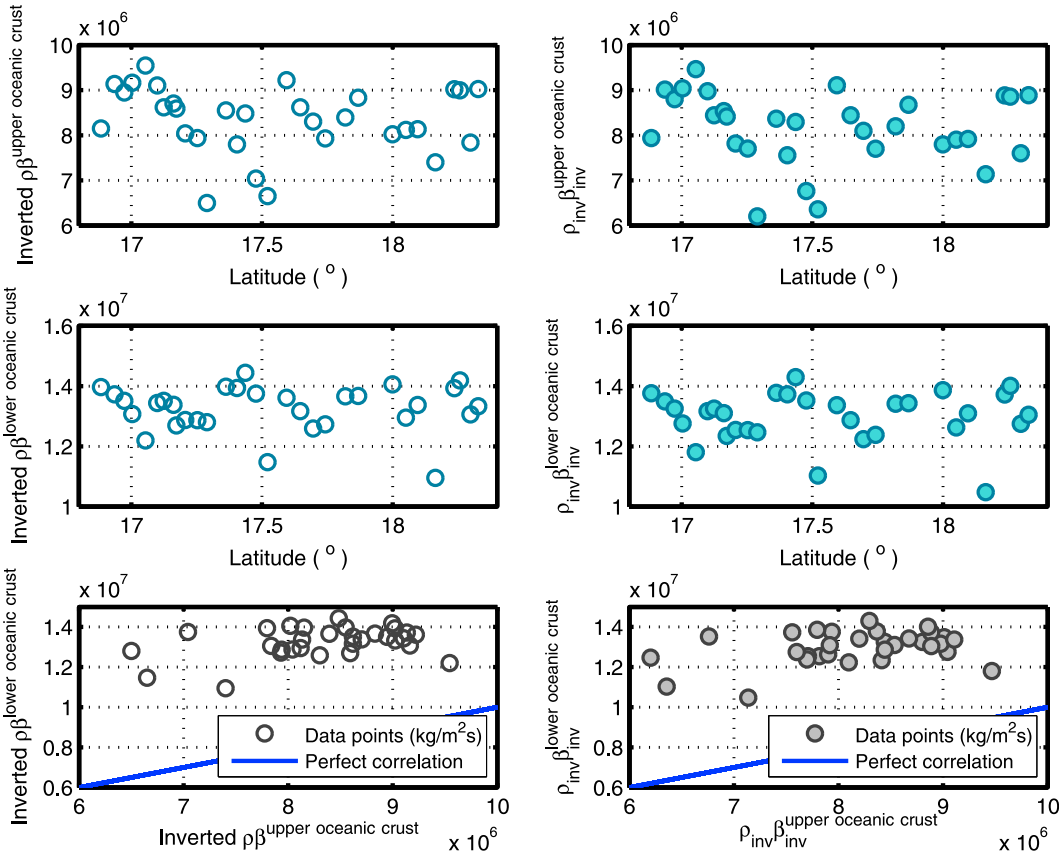

Figure 14. Comparison between (left) the inverted impedance and (right) the product of inverted S wave velocity and density for the upper and lower oceanic crust. (bottom) Linear correlation plots showing that the impedance for the upper oceanic crust and that for the lower oceanic crust are not correlated.

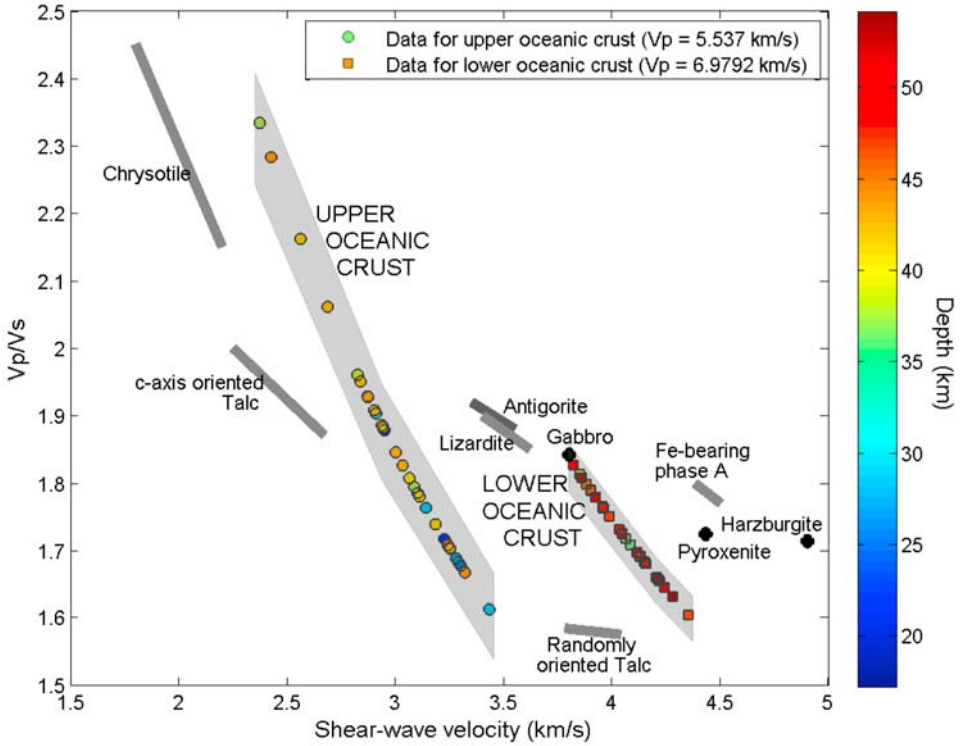

Figure 15. Calculated Vp/Vs ratio versus S wave velocity (Vs) at a depth of 35 km and a range of likely temperatures (500–800°C) at this depth for candidate hydrated phases (gray lines) and rock types (black diamonds). The points for randomly oriented talc and c axis oriented talc are from *Mainprice et al.* [2008], and those for different rock types are from *Christensen and Salisbury* [1975]. The data points for the upper oceanic crust are highly varying in Vp/Vs and Vs domain (average Vp/Vs of 1.85) and lie close to talc phases, whereas those for the lower oceanic crust are tightly bounded (average of 1.72). The light gray shaded regions denote uncertainties due to the choice of Vp. The lower bound of the uncertainty for the upper oceanic crust is computed when Vp = 5.387 km/s, and the upper bound is when Vp = 5.689 km/s. The lower bound of the uncertainty for the lower oceanic crust is computed when Vp = 6.898 km/s, and the upper bound is when Vp = 7.06 km/s.

where T_0 denotes the amplitude arriving at the bottom of the layer, and the subscript indicates the travel path of converted P or S wave at each interface, numbered as 3 (mantle to lower oceanic crust), 2 (lower oceanic crust to upper oceanic crust), and 1 (upper oceanic crust to crust). To obtain the transmission response at the top and bottom of the oceanic crust, we divide the transmission coefficients for the case 2 and 3 by the case 1:

$$\frac{T^{\mathrm{CASE2}}}{T^{\mathrm{CASE1}}} = \frac{T_0 T_{P3p2} T_{P2s1}}{T_0 T_{P3p2} T_{P2p1}} = \frac{T_{P2s1}}{T_{P2p1}} \sim T_{P2s1} \tag{4}$$

$$\frac{T^{\mathrm{CASE3}}}{T^{\mathrm{CASE1}}} = \frac{T_0 T_{P3s2} T_{S2s1}}{T_0 T_{P3p2} T_{P2p1}} = \frac{T_{P3s2} T_{S2s1}}{T_{P3p2} T_{P2p1}} \sim T_{P3s2}, \tag{5}$$

where T^{CASE1} is the transmitted response for P wave with no conversion at each interface. T_{P2s1} from equation (4) directly relates to the amplitude of negative (blue) RF pulse; T_{P3s2} from equation (5) is that of positive (red) RF pulse, shown in Figure 13.

[23] In the inversion, we use the linearized Zoeppritz equation, which describes the elastic, plane wave reflection and transmission coefficients between two half-spaces [*Aki and Richards*, 2002] for small incidence angles. The P-to-S transmission coefficient depends only on the S wave velocity and density variations,

$$T^{PS} = \frac{p\alpha}{2\cos j}\left[\left(1 - 2\beta^2 p^2 - 2\beta^2 \frac{\cos i}{\alpha}\frac{\cos j}{\beta}\right)\frac{\Delta\rho}{\rho} - 4\beta^2\left(p^2 + \frac{\cos i}{\alpha}\frac{\cos j}{\beta}\right)\frac{\Delta\beta}{\beta}\right], \tag{6}$$

where p represents the ray parameter, α the P wave velocity, β the S wave velocity, ρ the density, and i and j the incident and transmitted angle, respectively. Assuming the small angle approximation (thus $p^2 \rightarrow 0$), equation (6) is reduced as follows:

$$T^{PS} = \frac{p\alpha}{2}\left[\left(1 - \frac{2\beta}{\alpha}\right)\frac{\Delta\rho}{\rho} - \frac{4\beta}{\alpha}\frac{\Delta\beta}{\beta}\right]. \tag{7}$$

The approximation is valid for small angles which is suitable for conversions along the portion of the oceanic crust before the TMVB. In the inversion, we prescribe seismic parameters (α (or Vp), β (or Vs), and ρ) for the crust and mantle, and the P wave velocity of the upper and lower oceanic crust. Finally, we use least squares inversion to obtain the imped-

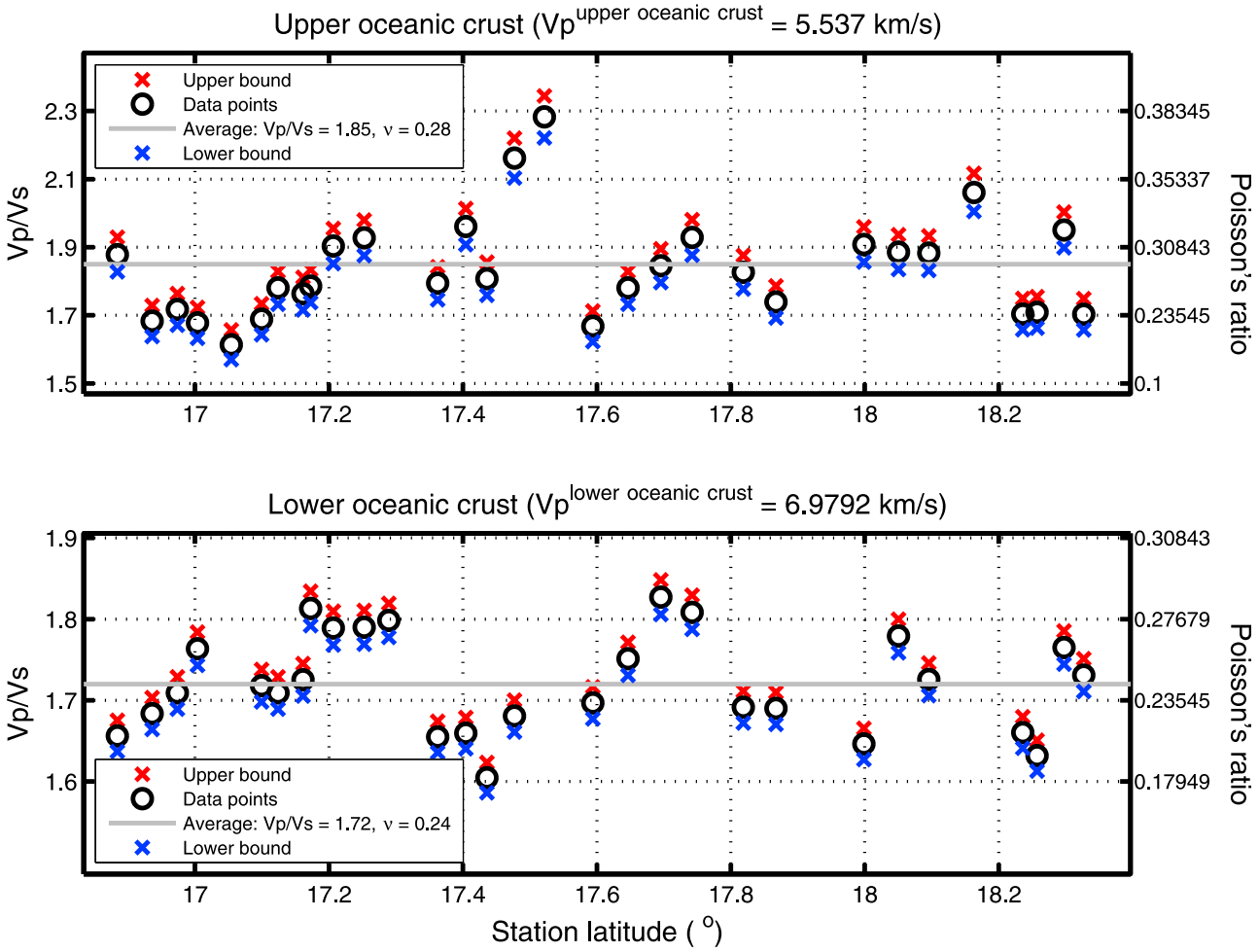

Figure 16. The Vp/Vs (left axis) and Poisson's (right axis) ratios versus station latitude. Note that the Vp/Vs and Poisson's ratios for the upper oceanic crust are highly variable (Vp/Vs of 1.6–2.3) along the array, whereas those for the lower oceanic crust are tightly bounded (Vp/Vs of 1.6–1.83). The lower bound of the uncertainty for the upper oceanic crust is computed when Vp = 5.387 km/s, and the upper bound is when Vp = 5.689 km/s. The average Vp/Vs ratio for the lower bound is 1.8, and that for the upper bound is 1.9. The lower bound of the uncertainty for the lower oceanic crust is computed when Vp = 6.898 km/s, and the upper bound is when Vp = 7.06 km/s. The average Vp/Vs ratio for the lower bound is 1.7, and that for the upper bound is 1.74.

ance (a product of S wave velocity and density) for the upper and lower oceanic crust. The data set for the inversion are the measured amplitude height of the negative and positive RF pulses normalized by the P wave pulse arriving at 0 s. In addition, the separation in time is used to invert for the thickness.

[24] We note that the inversion is mainly sensitive to the shear wave velocity variations and not density variations, and consequently S wave velocity and density are highly correlated to each other. The impedance values at the upper and lower oceanic crust are not correlated to each other (see Figure 14, bottom). The S wave velocity is, however, still useful because a product of separately inverted S wave velocity and density is consistent with the inverted impedance for the upper and lower oceanic crust as shown in Figure 14. Density variations along the array are moderate (2600–2750 kg/m^3 in the upper oceanic crust; 3125–3275 kg/m^3 in the lower oceanic crust). The inverted S wave velocity is extremely low and highly variable (2.4–3.4 km/s in the upper oceanic crust; 3.6–4.2 km/s in the lower oceanic crust). This S wave velocity is later used to compute Vp/Vs and Poisson's ratios with prescribed P wave velocities for the upper and lower oceanic crust. Since the Vp/Vs ratio strongly depends on the mean rheology of the oceanic crust, we use a range of P wave velocities for the oceanic crust that would give reasonable ratios. We did not attempt to independently measure the P wave velocity in the layer with multiples [*Audet et al.*, 2009] because they are very weak in the raw data.

[25] We further test and refine this set of P wave velocities by plotting the Vp/Vs ratio versus S wave velocity at a depth of 35 km and a range of likely temperatures at this depth for

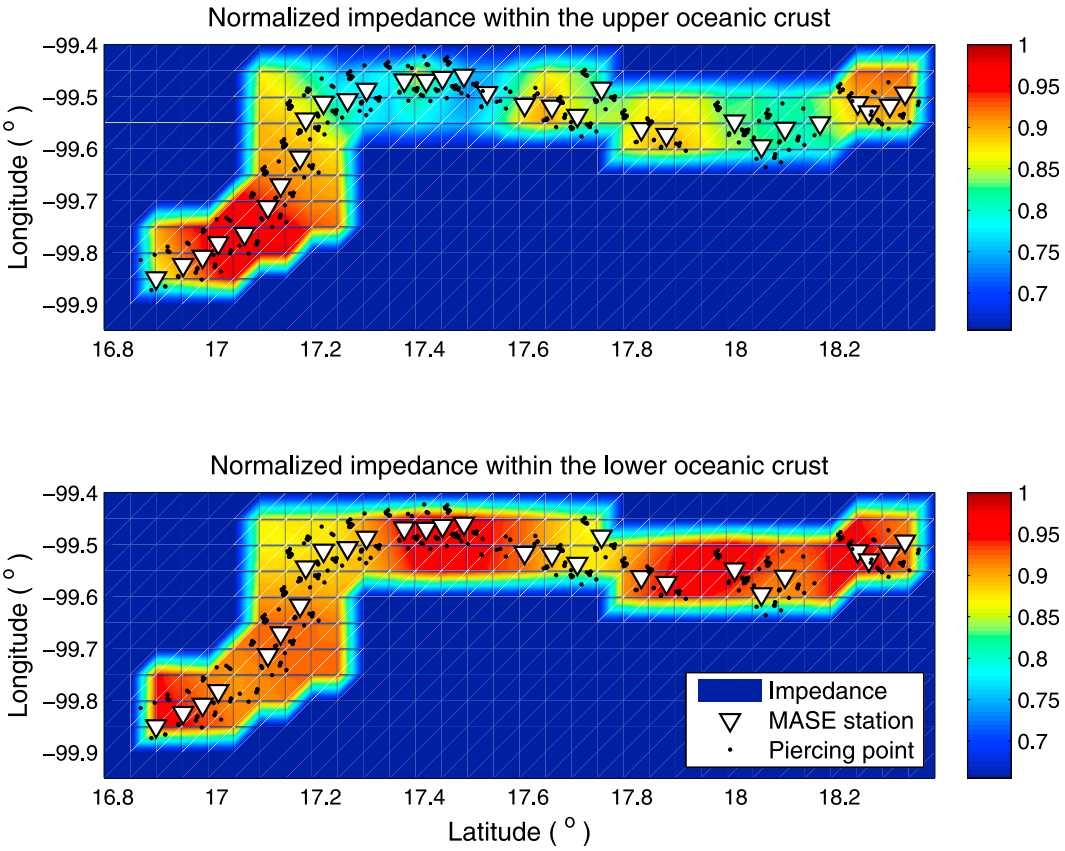

Figure 17. Variations in the (normalized) impedance within upper and lower oceanic crust along the MASE array south of the TMVB. The flat part of the oceanic crust starts at latitude of 17.2°. Each plot is generated using the nearest-neighbor interpolation scheme.

the candidate low-pressure hydrated phases in Figure 15. The mineral properties were calculated using finite strain theory [*Duffy and Anderson*, 1989] and recently reported velocities [*Pawley et al.*, 1995; *Bailey and Holloway*, 2000; *Reynard et al.*, 2007; *Mainprice et al.*, 2008; *Sanchez-Valle et al.*, 2008]. Data points corresponding to the upper oceanic crust are highly varying in the Vp/Vs versus Vs domain (average Vp/Vs of 1.85) whereas those to the lower oceanic crust are tightly bounded (average of 1.72). The uncertainty range, specified in Figures 15 and 16, is set such that the average of the data points for the upper oceanic crust lie between the Vp/Vs ratios of 1.8 and 1.9, and that for the lower oceanic crust between 1.7 and 1.74. Corresponding P wave velocity for the upper oceanic crust lies between 5.387 and 5.689 km/s (data points are plotted in Figures 15 and 16 when Vp = 5.537 km/s), and that for the lower oceanic crust lies between 6.898 and 7.06 km/s (data points are plotted in Figures 15 and 16 when Vp = 6.979 km/s).

[26] The data points for the upper oceanic crust are highly depth dependent and lie in between data obtained for preferentially oriented talc [*Bailey and Holloway*, 2000] and randomly oriented talc phases [*Mainprice et al.*, 2008] (Figure 15). The shallow depth (near the Pacific coast) corresponds to the lower Vp/Vs and Poisson's ratios (higher Vs), and the deeper depth of the subhorizontal part of the oceanic crust corresponds to the higher Vp/Vs and Poisson's ratios (lower Vs) (Figure 15). On the other hand, the data points for the lower oceanic crust lie close to hydrous phases like antigorite and lizardite. Gabbro is also capable of explaining the lower oceanic crust data. High-pressure hydrous phases, like Fe-bearing phase A and depleted mantle rocks, like pyroxenite and harzburgite, are characterized by higher Vs values than what we observe. This may imply that lower oceanic crust is unaltered one over the dry-depleted mantle rock.

[27] Inverted impedance (normalized by the maximum impedance) for all the off-axis piercing points is shown as a 2-D strip of variations along the array (Figure 17). The Vp/Vs and Poisson's ratios are plotted in a similar fashion to show the lateral variability for the upper and lower oceanic crust in a map view (Figures 18 and 19). In general, variably low impedance as well as highly variable Vp/Vs and Poisson's ratios (both due to extremely low S wave velocity) are observed at the flat part of the upper oceanic crust. On the other hand, the lateral variability of each seismic parameter is minimal along the array in the lower oceanic crust. The average impedance for the lower oceanic crust is computed to be 1.3172×10^7 kg/m^2/s.

[28] The time separation of the two converted phases is used to invert for the thickness of the oceanic crust. Figure 20 shows the thickness of the continental crust, oceanic crust and oceanic Moho. The thickness of the crust and oceanic Moho

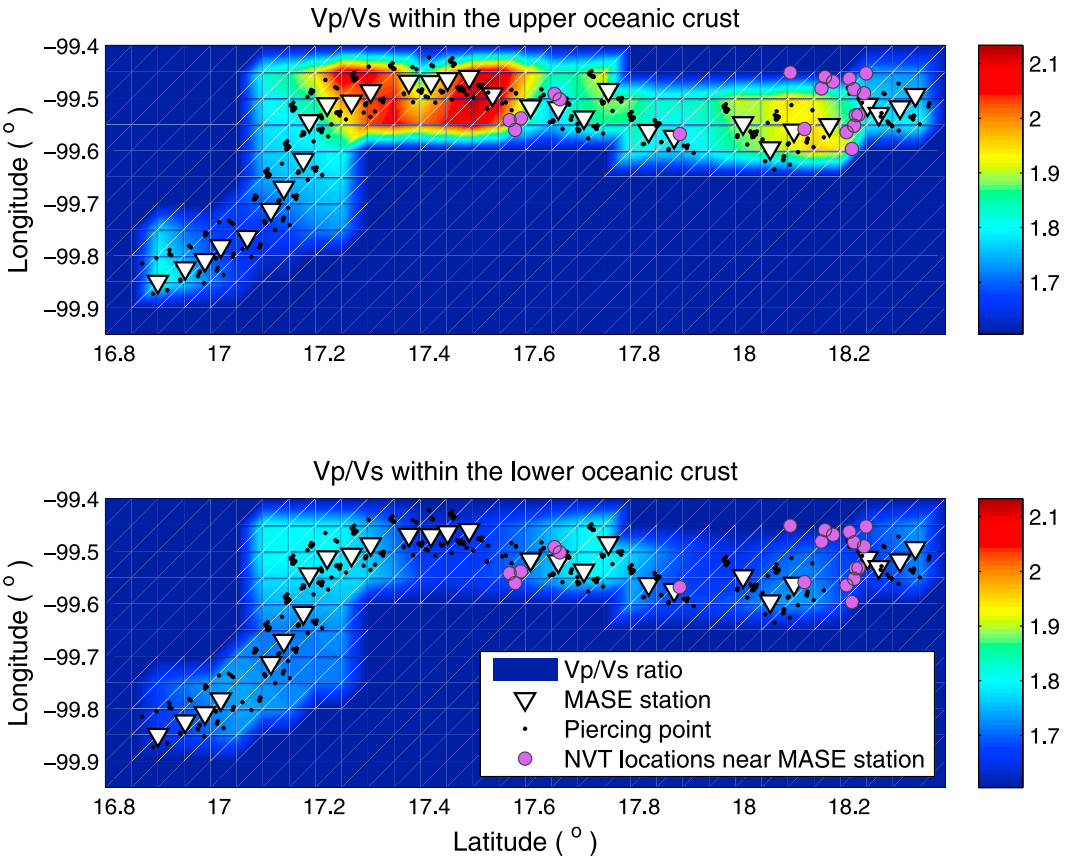

Figure 18. Variations in the Vp/Vs ratio within upper and lower oceanic crust along the MASE array south of the TMVB. The flat part of the oceanic crust starts at latitude of 17.2°. Each plot is generated using the nearest-neighbor interpolation scheme. The NVT locations that are located on a near the slab interface near the MASE stations are shown as purple circles.

agree well with our observation of shallow-to-horizontal interfaces shown in Figures 6 and 7. The thickness of the oceanic crust becomes gradually thicker as the slab dips at a shallow angle, and it becomes almost constant (1 or 2 km thinner away from the coast).

[29] We can further explore our data set to compute for the thickness of the upper and lower oceanic crust by using the FD modeling. In the modeling, we fix the thickness of the oceanic crust (8 km) and the seismic parameters (Vp, Vs, and ρ) for the lower oceanic crust because it is suggested to be generally homogeneous in composition as shown in Figures 15 and 16. We only vary the parameters (Vs, ρ, and thickness) for the upper oceanic crust, keeping the impedance the same as the previously inverted impedance. Figure 21 shows three P and S wave velocity models that would produce RF pulses with almost equal amplitude height corresponding to Pms and Pds phases. The thickness of the upper oceanic crust needs to be thicker as the S wave velocity increases: 3 km for the S wave velocity of 2.6 km/s, 4 km for 2.7 km/s, and 5 km for 2.8 km/s.

[30] Figure 22 shows our final model showing lateral variations in the seismic parameters (Vp/Vs and Poisson's ratios) with inverted thickness of the oceanic crust in a depth cross section. The thickness of the upper oceanic crust is set to 3 km from our FD modeling and inversion (Figures 11 and 21). The nonvolcanic tremor (NVT), specified in red squares, mostly occurs in the continental crust (5–40 km depth) with a few events localized on the horizontal plate interface or in the subducted plate crust [*Payero et al.*, 2008]. In addition, the slow slip events (SSEs) that occurred in 2006 coincide with our study area from Acapulco to a point 100 km to the north [*Larson et al.*, 2007].

3. Discussion

[31] The flat slab regions occur in 10% of modern convergent margins and have been studied in several places in the world (central Chile, Peru, SW Japan, etc.) [*Gutscher et al.*, 2000]. It is proposed that the flat subduction in most of places was formed primarily by the buoyancy of thickened oceanic crust and a delay in the basalt to eclogite transition due to the cool thermal structure of the overlying plate [*Gutscher et al.*, 2000]. Other proposals are plate velocity [*Lallemand et al.*, 2005], resistance to plate bending [*Schellart et al.*, 2007; *Schellart*, 2008], topographic asperities [*Gutscher*, 2002], and symmetry [*Gephart*, 1994]. It has also been suggested that there might be a direct relationship between flat slab subduction and silica enrichment in the continental lithosphere [*Wagner et al.*, 2008]. Of the flat subduction regions, the subduction system in central

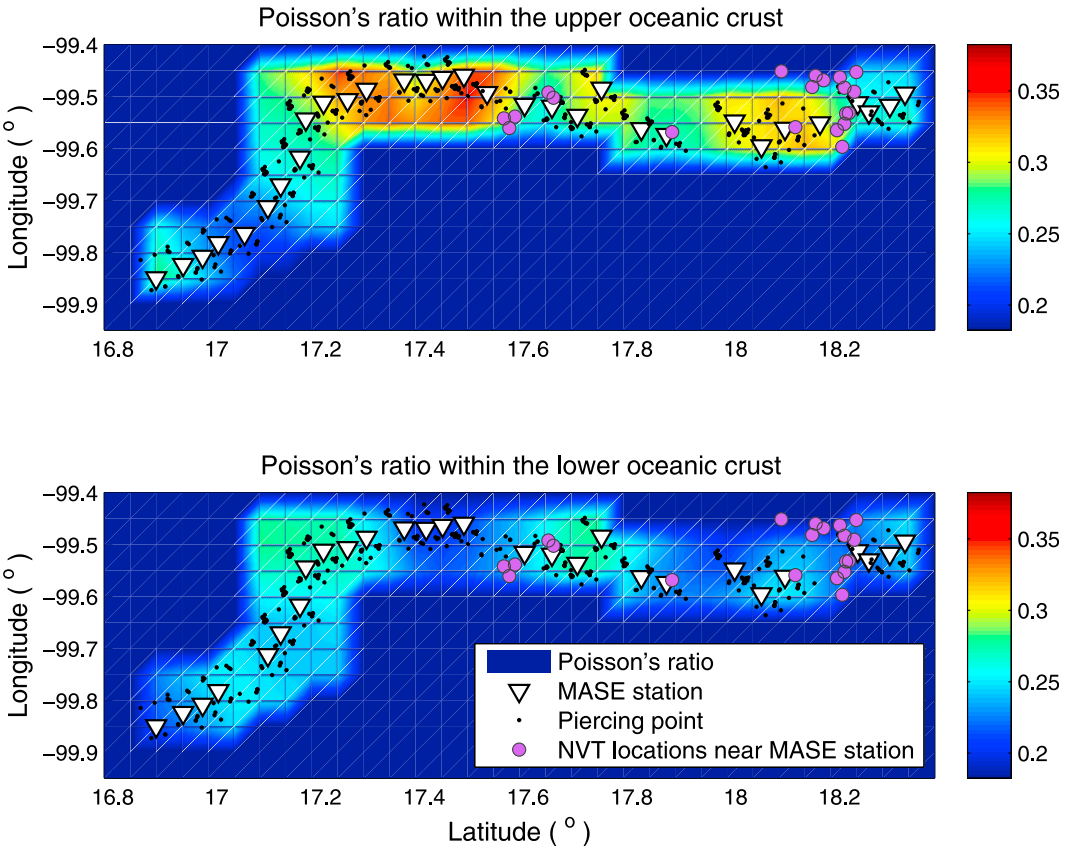

Figure 19. Variations in the Poisson's ratio within upper and lower oceanic crust along the MASE array south of the TMVB. The flat part of the oceanic crust starts at latitude of 17.2°. Each plot is generated using the nearest-neighbor interpolation scheme. The NVT locations that are located on a near the slab interface near the MASE stations are shown as purple circles.

Mexico is unique in a sense that the horizontal oceanic crust with normal crustal thickness is situated at a very shallow depth (~40 km) and the asthenosphere is absent [*Pérez-Campos et al.*, 2008]. Our RF analysis shows the oceanic crust is subducting in a shallow (15°) to horizontal dip, extending to 250 km from the MAT, and underneath the TMVB descending into the mantle in a very steep angle of 75°. Such unusual subduction geometry suggests that the central Mexico is in a slab rollback mode [*Pérez-Campos et al.*, 2008]. This is confirmed by the age progression of the volcanism [*Ferrari*, 2004]. An MT survey result [*Jödicke et al.*, 2006] also supports this idea based on a few isolated low-conductivity zones in the crust that they interpreted as episodes of slab dewatering as it rolls back.

[32] The thin low-velocity (S wave velocity of 2.4–3.4 km/s) layer on top of the oceanic crust at a shallow depth (~40 km) has important implications in the subduction history at central Mexico. If we assume the low-velocity layer is low strength, then this would explain the decoupling of the slab from the overriding plate despite the horizontal interface. The decoupling is evidenced by the lack of compressional structures in the last 20 Ma [*Nieto-Samaniego et al.*, 2006; *Morán-Zenteno et al.*, 2007]. Present GPS observations and the lack of compressional seismicity in the overlying plate also support this. *Manea and Gurnis* [2007] suggested that a thin channel of low velocity mantle above the oceanic crust is a remnant of the mantle wedge, and provided a numerical model to support the present slab configuration.

[33] Detailed mapping of inverted seismic parameters reveals that the upper oceanic crust is highly heterogeneous, and is composed of mechanically weak hydrous minerals (talc) on top of unaltered lower oceanic crust. The presence of such hydrous minerals in the oceanic crust reduces the seismic velocity to considerably less than the velocity of the surrounding mantle [*Kawakatsu and Watada*, 2007]. The hydrous minerals become unstable at pressure and temperature conditions at around 50 km at the shallow subduction system and are dehydrated to become anhydrous eclogitic oceanic crust [*Kawakatsu and Watada*, 2007]. Higher Vp/Vs and Poisson's ratios at the subhorizontal part of the oceanic crust at a depth of ~40 km imply the presence of more free water and thus an active dewatering process due to the serpentinization process. In addition, lateral variations in the impedance (especially S wave velocity) in the upper oceanic crust directly correspond to its variable thickness. On the other hand, the lower oceanic crust is less heterogeneous and suggested to be unaltered by water.

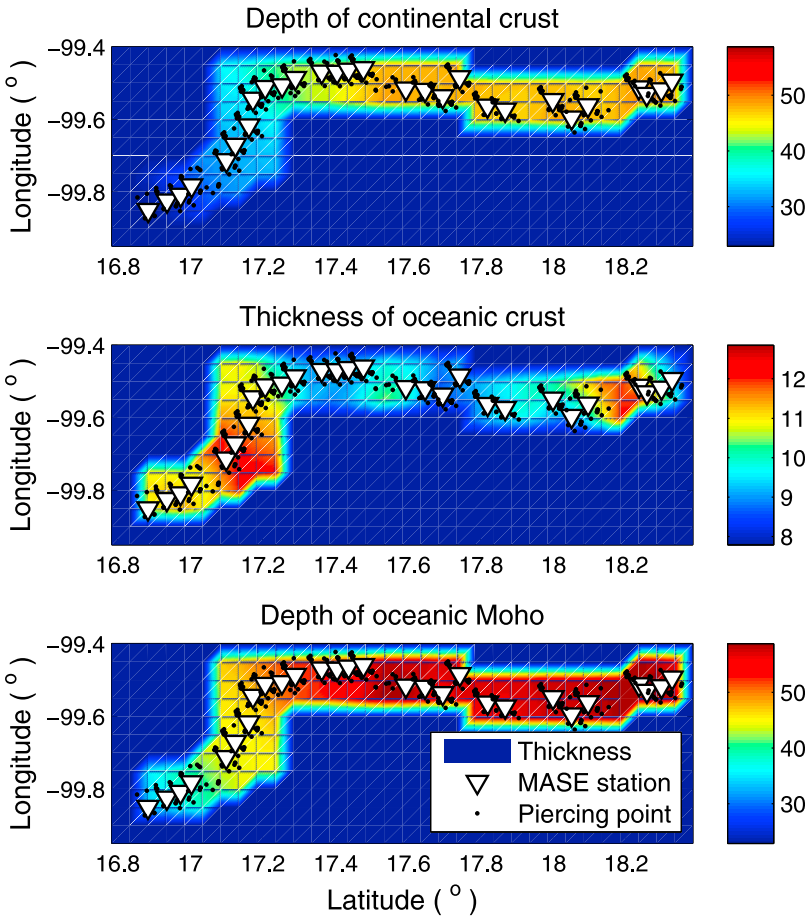

Figure 20. Thickness of the continental crust, oceanic crust, and oceanic Moho. We invert for the thickness of the continental crust and the oceanic crust by measuring the time difference between two RF pulses corresponding to Pds and Pms phases. Note that the thickness of the oceanic crust becomes gradually thicker as the slab dips at a shallow angle, and it becomes almost constant and 2 or 3 km thinner in the flat slab region (after the latitude of 17.2°). The slab thickens before it plunges into the mantle. Each plot is generated using the nearest-neighbor interpolation scheme.

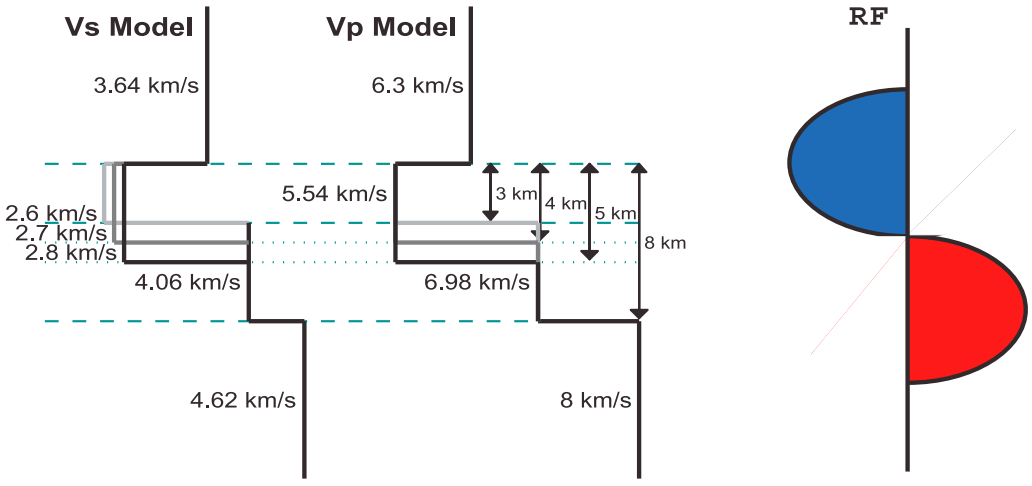

Figure 21. Velocity models that produce RF pulses with the equal amplitude height and opposite polarity corresponding to Pms and Pds phases. In the FD modeling, we only vary the S wave velocity, density, and thickness of the upper oceanic crust.

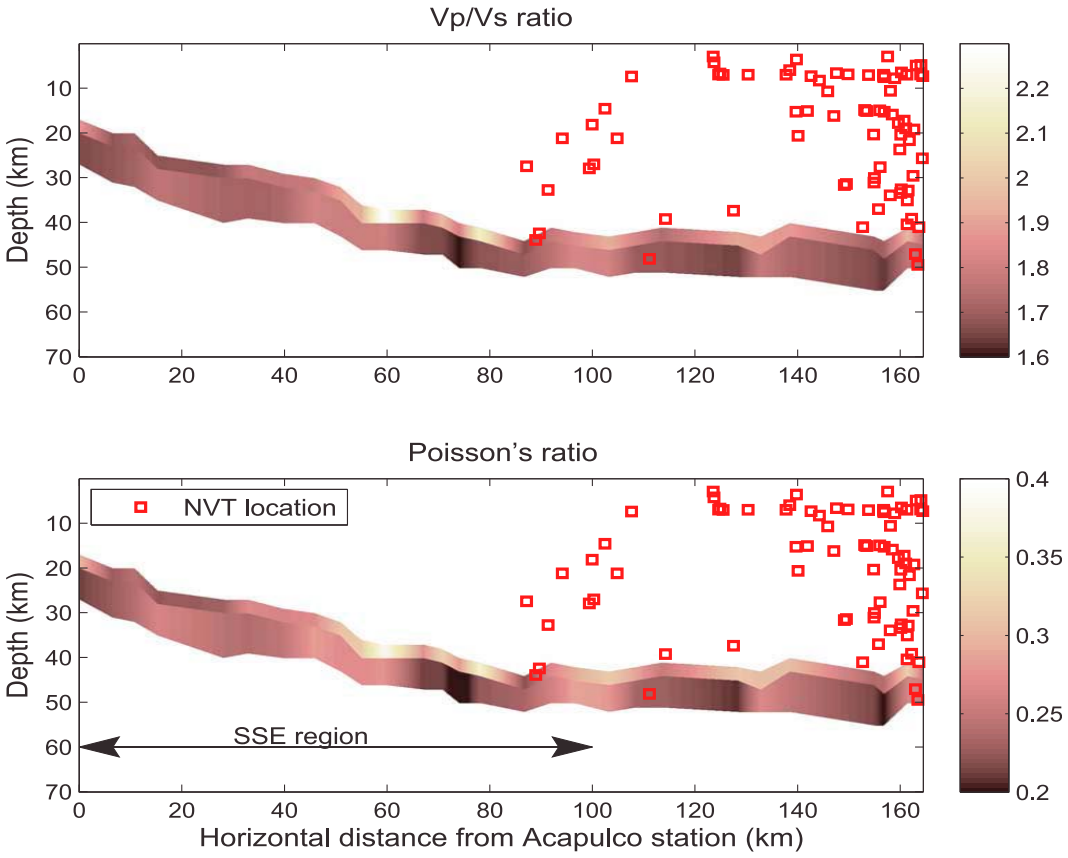

Figure 22. Final model including the (top) Vp/Vs and (bottom) Poisson's ratios of the subducted oceanic crust. The upper oceanic crust region has rapidly variable values (high Vp/Vs and Poisson's ratios on average) as opposed to the lower oceanic crust with moderately variable seismic properties. Most of the NVTs are located above the oceanic crust (a very few points inside the oceanic crust). The 2006 SSEs extend from the coast near Acapulco to a point 100 km to the north [*Larson et al.*, 2007].

[34] Our interpretation on the low-velocity layer on top of the subducting Cocos plate can be correlated to the recent observations on the NVT and SSEs in central Meixco. Recent studies of episodic tremor and slip (ETS) in both Cascadia and Japan point to an origin that involves fluids near the plate boundary [*Audet et al.*, 2009; *Rubinstein et al.*, 2010]. In particular, the NVT is a result of fluid flow and fluid processes at the plate interface and within the overlying plate [*Rubinstein et al.*, 2010]. The NVT coincides with the place within and above the subducting oceanic crust where the fluid content is suggested to be high. If the NVT is within the layer, then it is likely due to fluid motion. If it is above, it is likely due to fluid escaping from the interface into the continental crust. Furthermore, most slow slip patches coincide with the presence of the very low velocity layer on top of the oceanic crust [*Larson et al.*, 2007].

[35] High pore pressure might be in part responsible for anomalously low S wave velocity in the flat slab region which directly points to elevated Vp/Vs and Poisson's ratios in central Mexico [*Audet et al.*, 2009; *Christensen*, 1984; *Kawakatsu and Watada*, 2007; *Kodaira et al.*, 2004; *Van Avendonk et al.*, 2010]. The thin (slab-parallel) layer characterized by depressed absolute velocities, and high Vp/Vs and Poission's ratios are also seen in other subduction systems in SW Japan, Cascadia, and Costa Rica. *Christensen* [1984] explained that the zone of high pore fluid pressure might be the cause of the high Poisson's ratio in the subducted crust based on the laboratory measurements of the P and S wave velocities as a function of confining pressure and pore pressure for oceanic crust (basalt) samples. In his experiment, the data shows that decreases in seismic velocities accompany increasing pore pressure in oceanic rocks at fixed confining pressure. Thermal models provided by *Manea et al.* [2004] indicate that temperature and pressure gradients are small in the flat slab region before the TMVB (at about 45 km in depth). This suggests that the added pore pressure and the presence of hydrous minerals might be one of key factors to explain the low S wave velocity (or high Poisson's ratio) in the horizontal part of the upper oceanic crust. Also, the friction across the slab interface may be further reduced by high fluid pressures as a result of metamorphic dehydration of the slab [*Van Avendonk et al.*, 2010]. The influence of the pore pressure on seismic velocities is however expected to be diminish with depth and is unlikely to be significant at lower

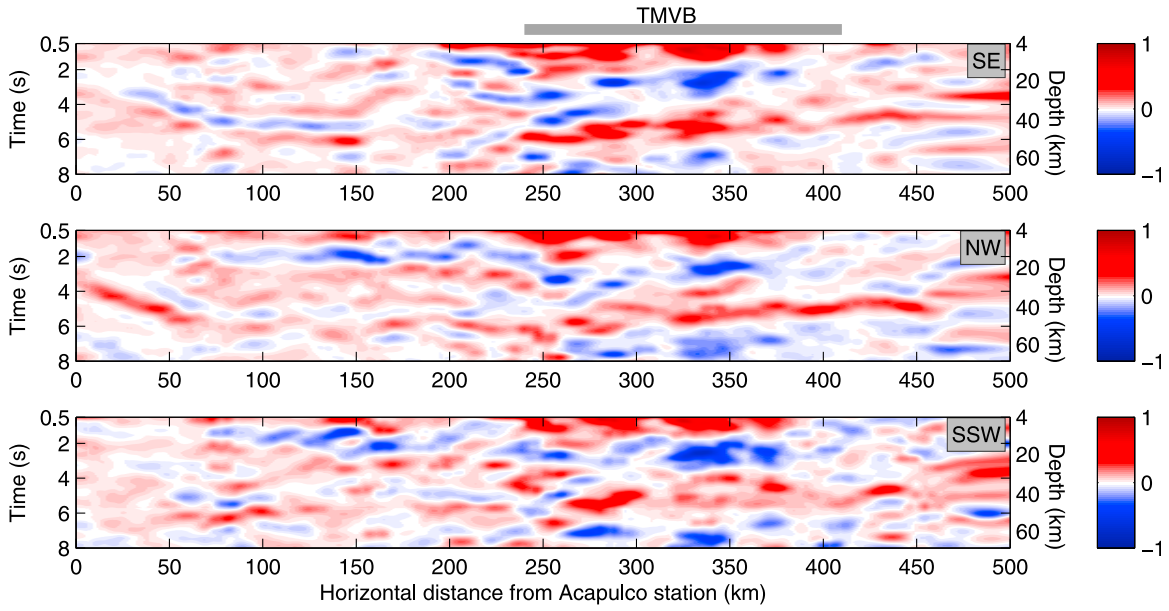

Figure A1. Stacked RF images without interpretation lines. Stacked RF images (uninterpreted) for (top) SE, (middle) NW, and (bottom) SSW back azimuths. The RFs are computed by the iterative time domain deconvolution [*Kikuchi and Kanamori*, 1982; *Ligorria and Ammon*, 1999]. Each image is created by assigning RF amplitudes into a separate output grid and filling the missing data by the linear interpolation. Note that the image is not sharply constrained from 450 km to the end of the array (~533 km) in the horizontal axis because the data are sparsely spaced at the northern section. The RFs in the SSW group are relatively noisier possibly because of the complications in the earthquake source and travel paths of seismic waves. Note that the P phase at zero seconds (the largest peak at the RF) is removed in the image to enhance the smaller signals after P. The color bar denotes the normalized RF amplitude. The interpreted display is given in Figure 7.

oceanic crustal depths where the porosity is extremely low [*Christensen*, 1984].

4. Conclusions

[36] We have produced an image of the subducted Cocos plate beneath central Mexico with RFs utilizing data from the MASE. Some key observations include the most detailed images of the Moho and oceanic crust from the RF analysis. The RFs show that the subducting oceanic crust is shallow, dipping to the north at 15° for 80 km from Acapulco and then horizontally underplates the continental crust for a distance of approximately 250 km from the MAT to the southern extent of the TMVB. The continental Moho is about 40 km deep beneath the TMVB and shallows toward the north. Beyond the flat subduction, the slab steeply subducts in 75° beneath the TMVB shown from our migrated image using the P-to-S converted phase, which agrees with the tomography result [*Pérez-Campos et al.*, 2008; *Husker and Davis*, 2009], although the steeply dipping slab beneath the TMVB is not shown from our raw RFs. Our dip sensitivity test using the FD modeling reveals that the RFs become unstable at very steep dip.

[37] The FD modeling result shows that we need a thin low-velocity layer (a thickness of 3 km; P wave velocity of 5.54 km/s; S wave velocity of 2.6 km/s) on top of the oceanic crust between the lower continental crust and the oceanic crust to explain the strong negative impedance contrast shown in 1 s RF data. We suspect that hydrous materials or high pore pressure are responsible for the low velocities observed. Furthermore, they are likely a major factor for sustaining our flat subduction geometry and also reducing the tectonic coupling of two plates for more than 20 Ma. Most of the NVT locations provided by *Payero et al.* [2008] are concentrated on the plate interface and the overlying crust, suggesting that the Cocos plate interface is an important pathway by which water is transported into the overlying crust. In particular, anomalously low S wave velocity in the upper oceanic crust deduced from our inversion directly points to elevated Vp/Vs and Poissons ratios, indicating that the layer contains highly heterogeneous, weak, and hydrous minerals (talc) on top of normal lower oceanic crust.

Appendix A: Uninterpreted RF Images

[38] This appendix provides uninterpreted versions of Figures 7 and 8. Figure A1 shows the whole line stacked for various azimuths. Figure A2 shows the region near the MAT.

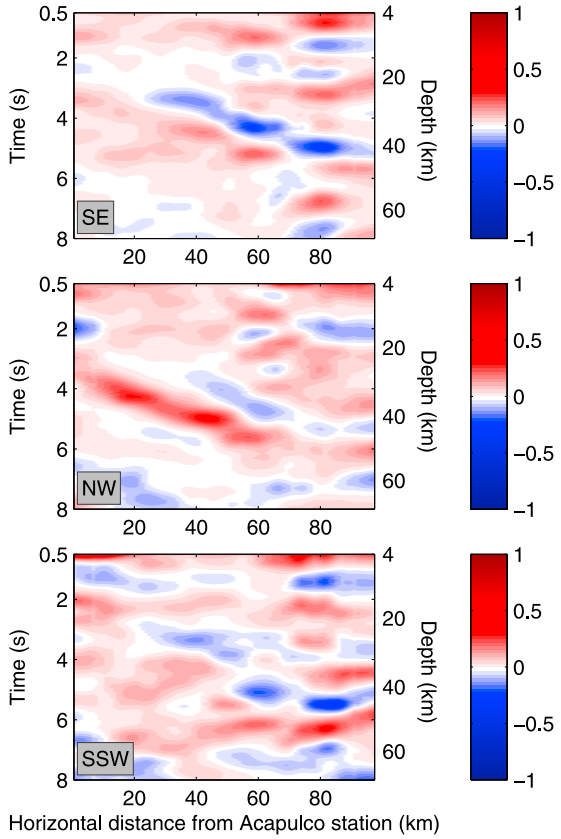

Figure A2. RF images showing the mechanism for the crust attenuation. RF images for (top) SE, (middle) NW, and (bottom) SSW back azimuths for 0.5–8 s and 0–95 km from the Acapulco station. Positive and negative RF amplitudes (indicated as dashed lines) above the subhorizontal oceanic crust are roughly parallel to its horizontal interface indicated as dark gray lines and not the shallow dipping oceanic crust indicated as light gray lines. The mechanism for such crust attenuation near the coast is thus determined to be undersided erosion by the oceanic crust and not uplift by the slab followed by the surface erosion. The color bar denotes the normalized RF amplitude. The interpreted display is given in Figure 8.

[39] **Acknowledgments.** This study was supported by the Gordon and Betty Moore Foundation through the Tectonics Observatory at Caltech and NSF award EAR 0609707. We thank Juan S. Payero for providing the NVT locations and the many volunteers who worked on the MASE experiment. This is contribution 108 from the Caltech Tectonics Observatory.

References

Aki, K., and P. G. Richards (2002), *Quantitative Seismology*, 2nd ed., Univ. Sci. Books, Sausalito, Calif.

Ammon, C. J. (1991), The isolation of receiver effects from teleseismic P waveforms, *Bull. Seismol. Soc. Am.*, *81*, 2501–2510.

Ammon, C. J., G. E. Randall, and G. Zandt (1990), On the nonuniqueness of receiver function inversions, *J. Geophys. Res.*, *95*(B10), 15,303–15,318, doi:10.1029/JB095iB10p15303.

Audet, P., M. G. Bostock, N. I. Christensen, and S. M. Peacock (2009), Seismic evidence for overpressured subducted oceanic crust and megathrust fault sealing, *Nature*, *457*, 76–78, doi:10.1038/nature07650.

Bailey, W., and J. R. Holloway (2000), Experimental determination of elastic properties of talc to 800°C, 0.5 GPa; calculations of the effect on hydrated peridotite, and implications for cold subduction zones, *Earth Planet. Sci. Lett.*, *183*, 487–498, doi:10.1016/S0012-821X(00)00288-0.

Bostock, M. G., S. Rondenay, and J. Shragge (2001), Multiparameter two-dimensional inversion of scattered teleseismic body waves: 1. Theory for oblique incidence, *J. Geophys. Res.*, *106*(B12), 30,771–30,782, doi:10.1029/2001JB000330.

Bostock, M. G., R. D. Hyndman, S. J. Rondenay, and S. Peacock (2002), An inverted continental Moho and the serpentinization of the forearc mantle, *Nature*, *417*, 536–538, doi:10.1038/417536a.

Christensen, N. I. (1984), Pore pressure and oceanic crustal seismic structure, *Geophys. J. R. Astron. Soc.*, *79*, 411–423.

Christensen, N. I., and M. H. Salisbury (1975), Structure and constitution of the lower oceanic crust, *Rev. Geophys. Space Phys.*, *13*, 57–86, doi:10.1029/RG013i001p00057.

Couch, R., and S. Woodcock (1981), Gravity and structure of the continental margins of southwestern Mexico and northwestern Guatemala, *J. Geophys. Res.*, *86*(B3), 1829–1840, doi:10.1029/JB086iB03p01829.

Duffy, T. S., and D. L. Anderson (1989), Seismic velocities in mantle minerals and the mineralogy of the upper mantle, *J. Geophys. Res.*, *94*(B2), 1895–1912, doi:10.1029/JB094iB02p01895.

Ferrari, L. (2004), Slab detachment control on mafic volcanic pulse and mantle heterogeneity in central Mexico, *Geology*, *32*, 77–80, doi:10.1130/G19887.1.

Ferrari, L., C. M. Petrone, and L. Francalanci (2001), Generation of oceanic-island basalt-type volcanism in the western Trans-Mexican volcanic belt by slab rollback, asthenosphere infiltration, and variable flux melting, *Geology*, *29*, 507–510, doi:10.1130/0091-7613(2001)029<0507:GOOIBT>42.0.CO;2.

Gephart, J. W. (1994), Topography and subduction geometry in the central Andes: clues to the mechanics of a noncollisional orogen, *J. Geophys. Res.*, *99*(B6), 12,279–12,288, doi:10.1029/94JB00129.

Gómez-Tuena, A., L. Mori, N. E. Rincon-Herrera, F. Ortega-Gutierrez, J. Sole, and A. Iriondo (2008), The origin of a primitive trondhjemite from the Trans-Mexican volcanic belt and its implications for the construction of a modern continental arc, *Geology*, *36*, 471–474, doi:10.1130/G24687A.1.

Gorbatov, A., and Y. Fukao (2005), Tomographic search for missing link between the ancient Farallon subduction and the present Cocos subduction, *Geophys. J. Int.*, *160*, 849–854, doi:10.1111/j.1365-246X.2005.02507.x.

Greene, F. (2009), Geometriía de la placa de Cocos usando funciones receptor a lo largo de la línea MASE, M.S. thesis, 34 pp., Univ. Nac. Autón. de México, Mexico City, June.

Gutscher, M.-A. (2002), Andean subduction styles and their effect on thermal structure and interplate coupling, *J. South Am. Earth Sci.*, *15*, 3–10, doi:10.1016/S0895-9811(02)00002-0.

Gutscher, M.-A., W. Spakman, H. Bijwaard, and E. R. Engdahl (2000), Geodynamics of flat subduction: Seismicity and tomographic constraints from the Andean margin, *Tectonics*, *19*, 814–833, doi:10.1029/1999TC001152.

Husker, A., and P. M. Davis (2009), Tomography and thermal state of the Cocos plate subduction beneath Mexico City, *J. Geophys. Res.*, *114*, B04306, doi:10.1029/2008JB006039.

Iglesias, A., R. W. Clayton, X. Perez-Campos, S. K. Singh, J. F. Pacheco, D. Garcia, and C. Valdes-Gonzalez (2010), S wave velocity structure below central Mexico using high-resolution surface wave tomography, *J. Geophys. Res.*, doi:10.1029/2009JB006332, in press.

Jödicke, H., A. Jording, L. Ferrari, J. Arzate, K. Mezger, and L. Rüpke (2006), Fluid release from the subducted Cocos plate and partial melting of the crust deduced from magnetotelluric studies in southern Mexico: Implications for the generation of volcanism and subduction dynamics, *J. Geophys. Res.*, *111*, B08102, doi:10.1029/2005JB003739.

Jording, A., L. Ferrari, J. Arzate, and H. Jödicke (2000), Crustal variations and terrane boundaries in southern Mexico as imaged by magnetotelluric transfer functions, *Tectonophysics*, *327*, 1–13, doi:10.1016/S0040-1951(00)00166-9.

Kawakatsu, H., and S. Watada (2007), Seismic evidence for deep-water transportation in the mantle, *Science*, *316*, 1468–1471, doi:10.1126/science.1140855.

Kay, R. W. (1978), Aleutian magnesian andesites: Melts from subducted Pacific Ocean crust, *J. Volcanol. Geotherm. Res.*, *4*, 117–132, doi:10.1016/0377-0273(78)90032-X.

Kikuchi, M., and H. Kanamori (1982), Inversion of complex body waves, *Bull. Seismol. Soc. Am.*, *71*, 491–506.

Kodaira, S., T. Iidaka, A. Kato, J. Park, T. Iwasaki, and Y. Kaneda (2004), High pore fluid pressure may cause silent slip in the Nankai Trough, *Science*, *304*, 1295–1298, doi:10.1126/science.1096535.

Kostoglodov, V., S. K. Singh, J. A. Santiago, S. I. Franco, K. M. Larson, A. R. Lowry, and R. Bilham (2003), A large silent earthquake in the

Guerrero seismic gap, Mexico, *Geophys. Res. Lett.*, *30*(15), 1807, doi:10.1029/2003GL017219.

Lallemand, S., A. Heuret, and D. Boutelier (2005), On the relationships between slab dip, back-arc stress, upper plate absolute motion, and crustal nature in subduction zones, *Geochem. Geophys. Geosyst.*, *6*, Q09006, doi:10.1029/2005GC000917.

Langston, C. A. (1979), Structure under Mount Rainier, Washington, inferred from teleseismic body waves, *J. Geophys. Res.*, *84*(B9), 4749–4762, doi:10.1029/JB084iB09p04749.

Larson, K., V. Kostoglodov, S. Miyazaki, and J. A. S. Santiago (2007), The 2006 aseismic slow slip event in Guerrero, Mexico: New results from GPS, *Geophys. Res. Lett.*, *34*, L13309, doi:10.1029/2007GL029912.

Ligorria, J. P., and C. J. Ammon (1999), Iterative deconvolution and receiver function estimation, *Bull. Seismol. Soc. Am.*, *89*, 19–36.

Mainprice, D., Y. Le Page, J. Rodgers, and P. Jouanna (2008), Ab initio elastic properties of talk from 0 to 12 GPa: Interpretation of seismic velocities at mantle pressures and prediction of auxetic behaviour at low pressure, *Earth Planet. Sci. Lett.*, *274*, 327–338, doi:10.1016/j.epsl.2008.07.047.

Manea, V. C., and M. Gurnis (2007), Subduction zone evolution and low viscosity wedges and channels, *Earth Planet. Sci. Lett.*, *264*, 22–45, doi:10.1016/j.epsl.2007.08.030.

Manea, V. C., M. Manea, V. Kostoglodov, C. A. Currie, and G. Sewell (2004), Thermal structure, coupling and metamorphism in the Mexican subduction zone beneath Guerrero, *Geophys. J. Int.*, *158*, doi:10.1111/j.1365-246X.2004.02325.x.

Morán-Zenteno, D. J., M. Cerca, and J. D. Keppie (2007), The Cenozoic tectonic and magmatic evolution of southwestern Mexico: Advances and problem interpretation, in Geology of Mexico, Celebrating the Centenary of the Geological Society of Mexico, edited by S. A. Alaniz-Álvarez and Á. F. Nieto-Samanieto, *Spec. Pap. Geol. Soc. Am.*, *422*, 71–91.

Müller, R. D., M. Sdrolias, C. Gaina, and W. R. Roest (2008), Age, spreading rates, and spreading asymmetry of the world's ocean crust, *Geochem. Geophys. Geosyst.*, *9*, Q04006, doi:10.1029/2007GC001743.

Nieto-Samaniego, A. F., A. S. Alaniz-Álvarez, G. Silva-Romo, M. H. Eguiza-Castro, and C. Mendoza-Rosales (2006), Latest Cretaceous to Miocene deformation events in the eastern Sierra Madre del Sur, Mexico, inferred from the geometry and age of major structures, *Geol. Soc. Am. Bull.*, *118*, 238–252, doi:10.1130/B25730.1.

Pardo, M., and G. Suárez (1995), Shape of the subducted Rivera and Cocos plates in southern Mexico: Seismic and tectonic implications, *J. Geophys. Res.*, *100*(B7), 12,357–12,373, doi:10.1029/95JB00919.

Pawley, A. R., S. A. T. Redfern, and B. J. Wood (1995), Thermal expansivities and compressibilities of hydrous phases in the system MgO-SiO_2-H_2O: Talc, phase A and 10-A phase, *Contrib. Mineral. Petrol.*, *122*, 301–307, doi:10.1007/s004100050129.

Payero, J. S., V. Kostoglodov, N. Shapiro, T. Mikumo, A. Iglesias, X. Pérez-Campos, and R. W. Clayton (2008), Nonvolcanic tremor observed in the Mexican subduction zone, *Geophys. Res. Lett.*, *35*, L07305, doi:10.1029/2007GL032877.

Pérez-Campos, X., Y. Kim, A. Husker, P. M. Davis, R. W. Clayton, A. Iglesias, J. F. Pacheco, S. K. Singh, V. C. Manea, and M. Gurnis (2008), Horizontal subduction and truncation of the Cocos Plate beneath central Mexico, *Geophys. Res. Lett.*, *35*, L18303, doi:10.1029/2008GL035127.

Reynard, B., N. Hilairet, E. Balan, and M. Lazzeri (2007), Elasticity of serpentines and extensive serpentinization in subduction zones, *Geophys. Res. Lett.*, *34*, L13307, doi:10.1029/2007GL030176.

Rubinstein, J. L., D. R. Shelly, and W. L. Ellsworth (2010), Non-volcanic tremor: A window into the roots of fault zones, in *New Frontiers in Integrated Solid Earth Sciences*, edited by S. Cloetingh and J. Negendank, pp. 287–314, Springer, Dordrecht, Netherlands.

Sanchez-Valle, C., S. V. Sinogeikin, J. R. Smyth, and J. D. Bass (2008), Sound velocities and elasticity of DHMS phase A to high pressure and implications for seismic velocities and anisotropy in subducted slabs, *Phys. Earth Planet. Inter.*, *170*, 229–239, doi:10.1016/j.pepi.2008.07.015.

Schellart, W. (2008), Overriding plate shortening and extension above subduction zones: a parametric study to explain formation of the Andes mountains, *Geol. Soc. Am. Bull.*, *120*(11), 1441–1454, doi:10.1130/B26360.1.

Schellart, W., J. Freeman, D. Stegman, L. Moresi, and D. May (2007), Evolution and diversity of subduction controlled by slab width, *Nature*, *446*, 308–311, doi:10.1038/nature05615.

Song, T.-R. A., D. V. Helmberger, M. R. Brudzinski, R. W. Clayton, P. Davis, X. Pérez-Campos, and S. K. Singh (2009), Subducting slab ultra-slow velocity layer conincident with silent earthquake in southern Mexico, *Science*, *324*, 502–506, doi:10.1126/science.1167595.

Valdes-Gonzalez, C., and R. P. Meyer (1996), Seismic structure between the Pacific coast and Mexico City from the Petatlan earthquake (M_s = 7.6) aftershocks, *Geofis. Int.*, *35*, 4377–4401.

Van Avendonk, H., W. S. Holbrook, D. Lizarralde, M. M. Mora, S. Harder, A. D. Bullock, G. E. Alvarado, and C. J. Ramirez (2010), Seismic evidence for fluids in fault zones on top of the subducting Cocos plate beneath Costa Rica, *Geophys. J. Int.*, *181*, 997–1016, doi:10.1111/j.1365-246X.2010.04552.x.

Wagner, L. S., M. L. Anderson, J. M. Jackson, S. L. Beck, and Z. Zandt (2008), Seismic evidence for orthopyroxene enrichment in the continental lithosphere, *Geology*, *36*, 935–938, doi:10.1130/G25108A.1.

Yan, Z., and R. W. Clayton (2007), Regional mapping of the crustal structure in southern California from receiver functions, *J. Geophys. Res.*, *112*, B05311, doi:10.1029/2006JB004622.

Zandt, G., and C. J. Ammon (1995), Continental crust composition constrained by measurements of crustal Poisson's ratio, *Nature*, *374*, 152–154, doi:10.1038/374152a0.

Zhu, L., and H. Kanamori (2000), Moho depth variation in southern California from teleseismic receiver functions, *J. Geophys. Res.*, *105*(B2), 2969–2980, doi:10.1029/1999JB900322.

R. W. Clayton, J. M. Jackson, and Y. Kim, Seismological Laboratory, California Institute of Technology, MC 252-21, Pasadena, CA 91125, USA. (ykim@gps.caltech.edu; clay@gps.caltech.edu)